Fractonic Chiral Plasma

Mixed Axial-Multipole Anomalies and Subdimensional Quantum Transport

Rihaan Shah

July 2026

Abstract

We construct and analyze a continuum and lattice framework for chiral matter subject to exact or emergent multipole conservation. The central result is that the coexistence of axial charge pumping and restricted mobility is not described by an ordinary chiral magnetic current alone. In a coframe-based dipole gauge formulation, the anomaly polynomial admits a mixed axial-dipole term

$$I_6 = \frac{1}{(2\pi)^3} F_5 \wedge \left[\frac{k_{VV}}{2} \mathcal{F} \wedge \mathcal{F} + \frac{k_{DD}}{2} \delta_{ab} F^a \wedge F^b + \frac{k_R}{24} \operatorname{tr}(R \wedge R) \right],$$

with anisotropic vector-dipole terms allowed only when a fixed spatial vector, foliation normal, or crystalline tensor is part of the background structure. The descent equations give anomalous Ward identities in which axial charge is converted into dipole and subdimensional transport channels. We prove a no-go theorem showing that exact scalar dipole conservation for a charged local fermion theory is incompatible with microscopic Lorentz invariance unless extra spatial structure, nonlocality, or additional constrained gauge fields are introduced. We then derive a mobility anomaly index from quantized dipole flux cycles, obtain anomaly-induced constitutive relations including a fractonic chiral magnetic tensor response, classify boundary and hinge inflow channels, and give an explicit constrained Wilson-fermion lattice construction. Reproducible Python calculations generate all figures, including spectral flow, hydrodynamic modes, real-time pumping, disorder sensitivity, boundary localization, and a minimal quantum-simulation circuit. The resulting universality class, a fractonic chiral plasma, is characterized by anomaly-induced mobility transmutation: axial pumping creates mobile dipoles, lineon currents, surface flows, and hinge modes rather than only an unrestricted vector current.

Contents

1 Introduction

Anomalous chiral transport is usually phrased in the language of mobile quasiparticles. In a relativistic plasma with vector gauge field A, axial background A_5, and field strength $F = \mathrm{d}A$, the Adler-Bell-Jackiw anomaly gives

$$\partial_\mu J_5^\mu = \frac{q^2}{16\pi^2}\epsilon^{\mu\nu\rho\sigma}F_{\mu\nu}F_{\rho\sigma} = \frac{q^2}{2\pi^2}\mathbf{E}\cdot\mathbf{B} \tag{1}$$

in the normalization used below. Once a chiral chemical potential is introduced, this anomaly constrains equilibrium and nonequilibrium coefficients such as the chiral magnetic and chiral separation effects [1, 2, 3, 4, 5, 6]. The current in these examples is an ordinary vector current. A charge created in the bulk can propagate through space, and the anomaly counts spectral flow between left and right handed states.

Fractonic matter changes the kinematic problem before dynamics are specified. A system that conserves charge and dipole moment cannot move a single isolated charge without changing the dipole moment. The local continuity equation takes the higher derivative form

$$\partial_t\rho + \partial_i\partial_j J^{ij} = 0, \tag{2}$$

where J^{ij} is a tensor current rather than a vector current. Dipoles, lineons, planons, and boundary composites can remain mobile even when the elementary charge is immobile [8, 9, 11, 13]. The question addressed in this paper is therefore concrete: what does axial anomaly pumping become when the produced charge cannot move as an ordinary vector current?

We call the resulting state a fractonic chiral plasma. This phrase means a many-body state, not a new microscopic ingredient. It denotes chiral degrees of freedom whose transport is constrained by exact or emergent multipole conservation. The central mechanism is anomaly-induced mobility transmutation: the anomaly produces charge in one symmetry sector, while the multipole constraints force the associated transport into a different mobility sector. Depending on background geometry and boundary orientation, the response may be a mobile dipole current, a lineon current, a surface dipole flow, a hinge-localized chiral channel, or a higher-rank tensor current.

The paper makes three main technical claims. First, exact scalar dipole conservation of an ordinary electric charge is not compatible with a local Lorentz-invariant fermion field theory unless additional background structure is supplied. The dipole charge $P^i = \int x^i\rho$ refers to a spatial slice and transforms noncovariantly under boosts. A continuum theory with exact dipole conservation must therefore be formulated using a preferred foliation, Aristotelian geometry, Newton-Cartan data, crystalline coframes, or an equivalent nonrelativistic structure. This is a no-go theorem, not an assumption.

Second, once the necessary spatial structure is included, a cohomological classification of mixed axial-dipole anomalies becomes possible. In a coframe formulation with vector-valued dipole gauge fields A^a and curvatures F^a, the anomaly polynomial contains an isotropic term $F_5 \wedge \delta_{ab}F^a \wedge F^b$. Terms of the form $F_5 \wedge F \wedge F^a$ require an invariant vector u_a or boundary normal and are absent

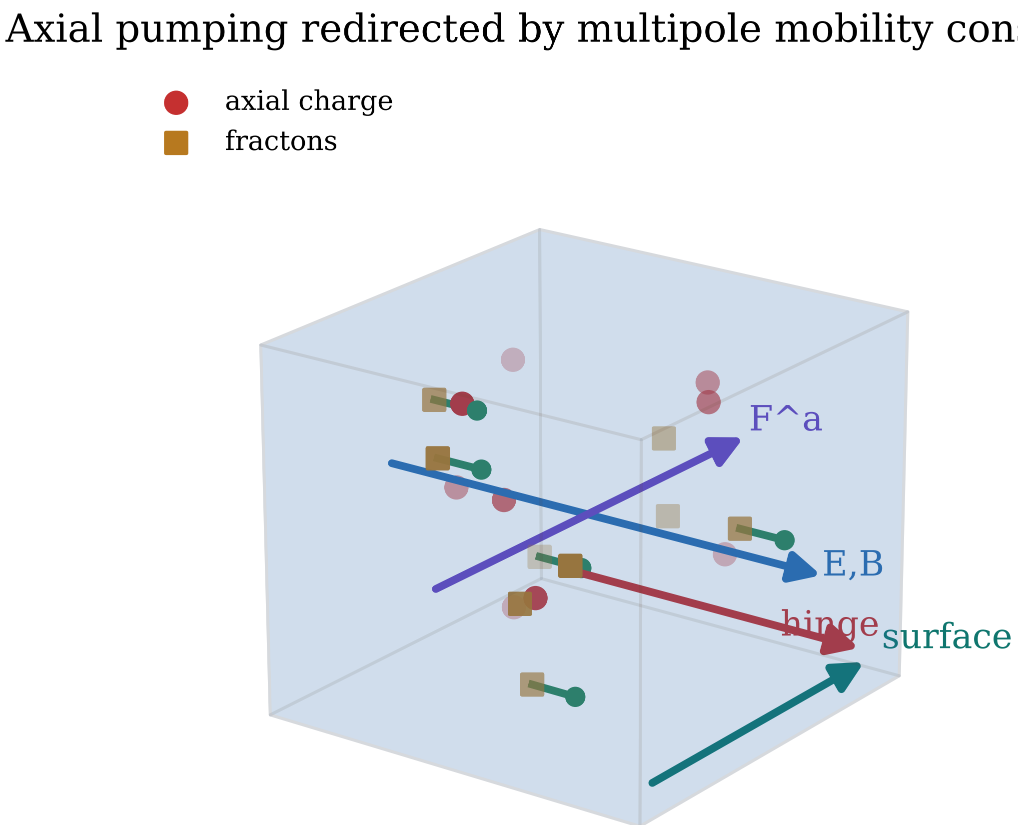

Figure 1: Visual abstract of a fractonic chiral plasma. The bulk medium carries chiral modes, ordinary electromagnetic fields, and vector-valued dipole gauge backgrounds. Axial pumping creates charge locally, but exact dipole conservation redirects transport into mobile dipoles, lineons, surface currents, and hinge channels. The rendering is schematic; the arrows encode the field and current directions used in the continuum definitions.

in a fully rotation-symmetric bulk. This distinction is essential: a formal tensor contraction is not automatically a genuine anomaly.

Third, the anomaly has transport consequences. The equilibrium generating functional and Kubo formulas imply a tensor response

$$J^{ij}_{\text{anom}} = \frac{k_{DD}}{2\pi^2}\,\mu_5\,\mathcal{B}^{ij} + \cdots \tag{3}$$

when the higher-rank magnetic field $\mathcal{B}^{ij}$ is the spatial representative of F^a in the scalar-charge sector. The dots denote dissipative and improvement terms fixed separately by hydrodynamics. The

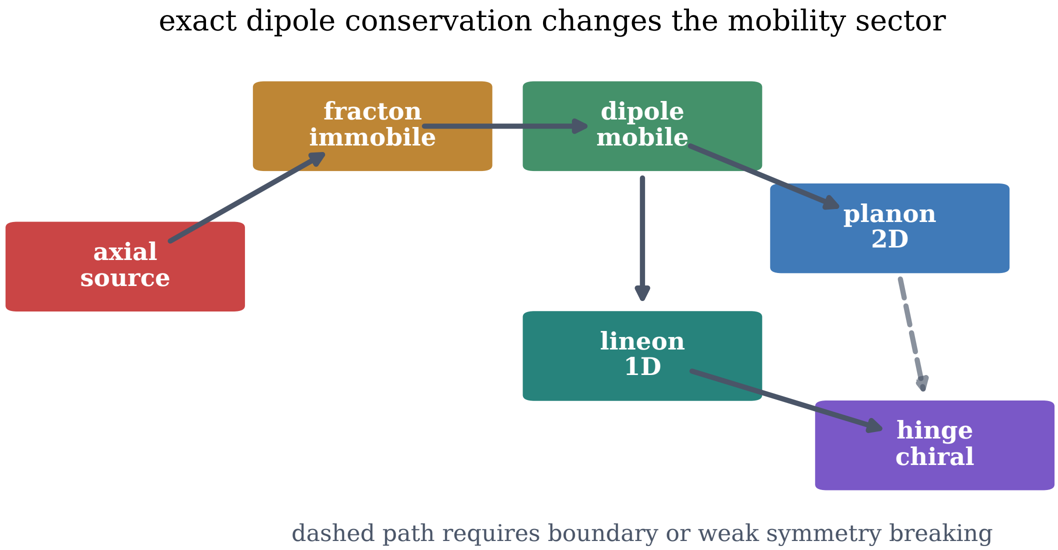

Figure 2: Mobility transmutation. The anomaly source creates axial charge locally. Multipole conservation decomposes the resulting response into immobile fractons, mobile dipoles, lineons, planons, and hinge currents. Solid arrows indicate channels required by exact Ward identities in the coframe theory. Dashed arrows indicate model-dependent relaxation channels allowed once weak symmetry breaking or boundaries are introduced.

coefficient is protected only under the same hypotheses that quantize the anomaly polynomial. In the symmetric tensor formulation without a coframe, the analogous $\mathcal{E}_{ij}\mathcal{B}^{ij}$ expression is not by itself a quantized ABJ anomaly. It can be a response term of a particular microscopic model, but it is not a universal local anomaly.

The computational part of the paper is deliberately modest. It does not claim to simulate a large microscopic material. Instead it implements controlled finite-dimensional models that reproduce the Ward identities and mobility selection rules. The code generates all figures, exports numerical arrays, verifies charge and dipole conservation on finite lattices, diagonalizes small spectral-flow Hamiltonians, integrates hydrodynamic mode equations, and constructs a minimal Trotter circuit that distinguishes ordinary current from dipole current.

The organization is as follows. Sections 2 and 3 audit neighboring literature and derive multipole conservation. Sections 4 and 5 define chiral matter and the two gauge-field languages. Section 6 classifies mixed anomalies by Fujikawa and descent methods. Sections 7 to 10 derive the mobility index, constitutive relations, fractonic chiral magnetic effect, and spectral-flow interpretation. Sections 11 and 12 treat anomaly inflow through boundaries and hinges. Sections 13 to 18 present the lattice model, hydrodynamics, nonequilibrium dynamics, numerical calculations, quantum-simulation protocol, and possible realizations. Sections 19 and 20 collect limitations, counterexamples, and conclusions.

2 Research Landscape and Novelty Audit

The ingredients of this paper are individually well developed. Chiral anomalies and anomaly-induced transport are classic results in quantum field theory and relativistic hydrodynamics [1, 2, 3, 4, 5]. Higher-rank $U(1)$ gauge theory, dipole conservation, and restricted mobility form the continuum language of many fracton phases [8, 9, 10, 11, 12]. More recent work has clarified curved-space fracton response, dipole Chern-Simons terms, anomalous dipole hydrodynamics, subsystem-symmetry anomalies, and quantum simulation routes [14, 15, 16, 17, 18, 19, 20, 21].

The present paper does not claim that fractons, chiral plasmas, anomaly inflow, quantum simulation, or higher-rank hydrodynamics are new. The narrower contribution is the analysis of a mixed axial-multipole anomaly that forces anomaly-generated chiral charge into higher-moment and subdimensional transport channels. The comparison in Table 1 summarizes the separation between prior ingredients and the object studied here.

Several lessons from this landscape determine the construction below. First, higher-rank gauge theories are not simply relativistic gauge theories with more indices. Their gauge transformations involve a preferred time direction or spatial differential operators. Second, anomaly polynomials are statements about differential forms on a specified background. A symbol such as $\mathcal{E}_{ij}\mathcal{B}^{ij}$ is not automatically a four-form density with quantized coefficient. Third, lattice realizations must face fermion doubling. A chiral continuum mode can appear at a boundary or as one member of a vectorlike lattice spectrum, but the full regulator must preserve the required gauge symmetries.

The manuscript uses the following terminology only where it is backed by equations. A mixed axial-multipole anomaly is a quantum obstruction to preserving axial symmetry and a multipole gauge symmetry simultaneously in a regulated path integral. A mobility anomaly index is an integrated anomaly invariant resolved by mobility sector. A fractonic chiral magnetic effect is a nondissipative tensor current induced by μ_5 and a generalized magnetic field when the equilibrium partition function and Kubo formula agree. In settings where these requirements fail, the terms are not used as claims.

3 Multipole Symmetries and Mobility Restrictions

Let $\rho(t, \mathbf{x})$ be a conserved scalar charge density on a d-dimensional spatial manifold with flat coordinates and boundary conditions chosen so that integrations by parts are valid. Charge and dipole moment are

$$Q = \int_\Sigma \mathrm{d}^d x\, \rho, \qquad P^i = \int_\Sigma \mathrm{d}^d x\, x^i \rho. \tag{4}$$

Reference class	Dimension	Symmetry	Gauge structure	Anomaly	Mobility	Difference from this work
ABJ and Fujikawa [1, 2, 3]	$3+1$	axial, vector	one-form A, A_5	$F \wedge F$	ordinary mobile charge	no dipole or subsystem constraint
Chiral magnetic hydrodynamics [4, 5]	$3+1$	vector, axial	one-form backgrounds	mixed gauge-gravity extensions	vector current	no tensor current or mobility sectors
Higher-rank $U(1)$ fractons [8, 9]	$d+1$	charge and dipole	symmetric tensor gauge fields	not axial	fracton, lineon, dipole	no chiral anomaly coefficient
Multipole symmetry EFT [11, 14]	non-rel.	polynomial shift, dipole	coframes, Newton-Cartan data	mostly kinematic	restricted by moments	not focused on axial spectral flow
Elasticity duality [10]	$2+1, 3+1$	translations, rotations	tensor gauge duals	defect response	disclinations and dislocations	no chiral plasma response
Dipole Chern-Simons and anomalous dipole fluids [15, 16]	$2+1, 3+1$	dipole $U(1)$	dipole gauge fields	dipole and boundary anomalies	dipole transport	axial $U(1)_5$ absent
Covariant fracton anomalies [17]	general	higher-rank, crystalline	covariant backgrounds	anomaly classification	restricted mobility	not tied to ABJ axial pumping
Subsystem-symmetry anomalies [18]	lattice and QFT	subsystem	foliated backgrounds	subsystem anomaly	planon and lineon sectors	no chiral magnetic analogue
Gapless fracton liquids [19]	$3+1$	emergent gauge symmetry	microscopic spin liquid	no axial anomaly	subdim. photons	not a chiral transport theory
Quantum simulations of anomalies [20, 21]	finite systems	gauge and chiral	digital or analog circuits	measured axial pumping	ordinary lattice channels	no exact multipole mobility filter

Table 1: Novelty audit. The proposed contribution is the conjunction of axial anomaly pumping with multipole-constrained mobility. The table is intentionally conservative. It identifies prior ingredients that the present construction uses, then states the narrower distinction.

Throughout this section, lowercase j^i denotes the ordinary spatial charge flux appearing in a vector continuity equation, uppercase $J^{ij} = J^{ji}$ denotes the symmetric rank-two tensor current whose double divergence transports charge in the scalar-charge sector, and J_5^μ denotes the axial four-current used in the anomalous Ward identity. The most general local continuity equation for charge is $\partial_t \rho + \partial_i j^i = 0$. Exact dipole conservation for arbitrary subregions imposes

$$0 = \frac{\mathrm{d}P^k}{\mathrm{d}t} = -\int_\Sigma \mathrm{d}^d x\, x^k \partial_i j^i = \int_\Sigma \mathrm{d}^d x\, j^k - \int_{\partial\Sigma} \mathrm{d}S_i\, x^k j^i. \tag{5}$$

For closed space or boundary conditions with vanishing flux moment, the integral of j^k must vanish for every allowed process. Locality then permits $j^i = \partial_j J^{ij}$, up to identically conserved curls. The continuity equation becomes

$$\partial_t \rho + \partial_i \partial_j J^{ij} = 0. \tag{6}$$

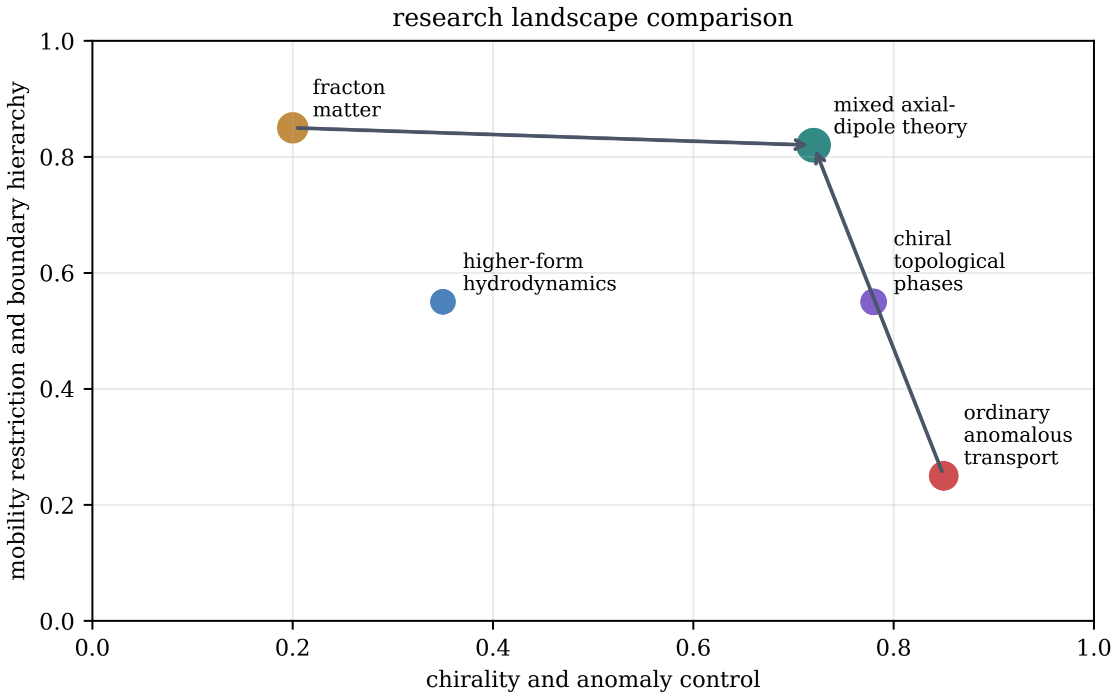

Figure 3: Research landscape comparison. The axes summarize chirality, anomaly control, mobility restriction, and boundary hierarchy. The proposed mixed-anomaly theory occupies the region where axial spectral flow, dipole gauge response, and subdimensional transport are simultaneously present. Coordinates are schematic but assigned from the symmetry content and transport mechanisms listed in Table 1.

Conversely, Eq. (6) conserves Q and P^i on a closed flat manifold because both $\int \partial_i \partial_j J^{ij}$ and $\int x^k \partial_i \partial_j J^{ij}$ reduce to boundary terms.

Equation (6) is the kinematic origin of immobility. Moving an isolated charge q from x^i to $x^i + a^i$ changes P^i by qa^i. The process is forbidden if P^i is exactly conserved. A neutral dipole made from charges $+q$ and $-q$ separated by ℓ^i can translate without changing total charge or total dipole moment. The dipole orientation may itself be conserved, so motion can be planar or line-like depending on the microscopic algebra. The same logic extends to quadrupole conservation, where even dipoles can become restricted and quadrupolar composites carry the lowest mobile moment.

On a lattice, P^i depends on the choice of origin. If $Q = 0$, a translation of the origin leaves P^i unchanged. If $Q \neq 0$, only dipole moment modulo QL_i is sharply defined on a periodic lattice of length L_i. This is why large dipole gauge transformations quantize fluxes and why a mobility index is naturally defined by cycles rather than by an absolute value of P^i. On an open lattice, boundary charge can absorb a dipole moment. A correct Ward identity must include boundary moment flux,

$$\frac{\mathrm{d}P^k}{\mathrm{d}t} = -\int_{\partial\Sigma} \mathrm{d}S_i \left(x^k \partial_j J^{ij} - J^{ik} \right). \tag{7}$$

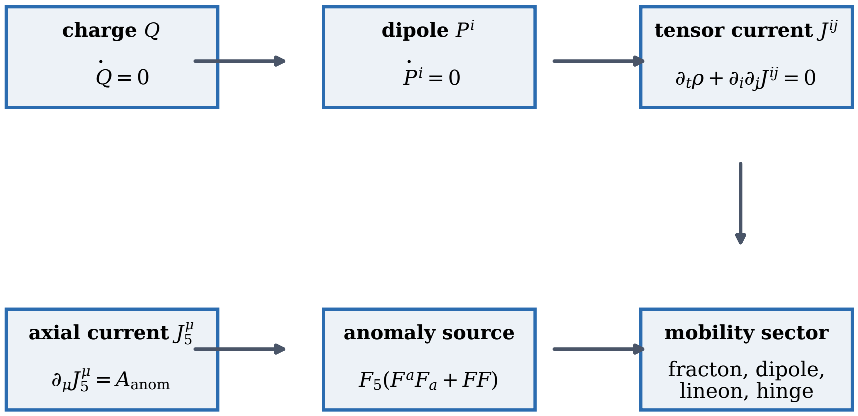

Figure 4: Symmetry and current hierarchy. Charge conservation gives a vector current. Charge plus dipole conservation forces that vector current to be a divergence of a tensor current. Axial symmetry is allowed to be anomalous, so its Ward identity contains a source made from ordinary and dipole gauge curvatures. The diagram distinguishes exact Ward identities from constitutive choices.

This term is central to the boundary anomaly cascade discussed later.

On curved manifolds there is no canonical coordinate x^i. A dipole charge must be defined using additional data: a flat crystalline coframe $e^a = e^a_i \mathrm{d}x^i$, a covariantly constant vector frame, or a foliation. Replacing $\partial_i \partial_j$ with two covariant derivatives is not innocuous because curvature makes their commutator nonzero. For a scalar density one may write

$$\partial_t \rho + D_i D_j J^{ij} = \mathcal{R}_{ij} J^{ij} + \text{torsion and boundary terms}, \tag{8}$$

unless improvement terms cancel the curvature contribution. Thus exact dipole conservation is usually a statement about a flat or crystalline background, while emergent dipole conservation can survive approximately at long wavelength.

It is important to distinguish several symmetry types. Scalar-charge fracton theories conserve charge and all components of dipole moment, with a symmetric tensor gauge field B_{ij}. Vector-charge theories conserve vector charge and angular moments, leading to lineon mobility. Subsystem symmetries conserve charge on lower-dimensional leaves such as planes or lines. Dipole symmetries can be treated as global polynomial-shift symmetries or as gauge-like redundancies once backgrounds are introduced. Higher-form symmetries act on extended operators and are not the same as dipole symmetries, although both can be represented by differential forms in special cases. The anomaly classification below keeps these distinctions explicit.

4 Chiral Matter and the Axial Anomaly

We begin with a vectorlike Dirac fermion decomposed into Weyl components ψ_χ, $\chi = \pm 1$, on a four-dimensional spacetime M_4. In the absence of multipole backgrounds the regulated Euclidean action is

$$S_\psi = \int_{M_4} \mathrm{d}^4 x \, e \, \bar{\psi} \, \mathrm{i}\gamma^\mu \left(\nabla_\mu + \mathrm{i}qA_\mu + \mathrm{i}q_5\gamma_5 A_{5\mu}\right)\psi. \tag{9}$$

The vector current is $J^\mu = \bar{\psi}\gamma^\mu\psi$, and the axial current is $J_5^\mu = \bar{\psi}\gamma^\mu\gamma_5\psi$. A gauge-invariant regulator preserves the vector Ward identity and assigns the anomaly to the axial Ward identity,

$$\nabla_\mu J_5^\mu = \frac{q^2}{16\pi^2}\epsilon^{\mu\nu\rho\sigma}F_{\mu\nu}F_{\rho\sigma} \; + \; \frac{1}{384\pi^2}\epsilon^{\mu\nu\rho\sigma}R^\alpha{}_{\beta\mu\nu}R^\beta{}_{\alpha\rho\sigma}. \tag{10}$$

The coefficient is fixed by the index of the Dirac operator and is unaffected by smooth interactions that do not close the gap of the regulator or break the protecting gauge symmetry.

The ordinary chiral magnetic effect follows from the same anomaly data plus equilibrium consistency. In a stationary background with axial chemical potential $\mu_5 = A_{5,0}$, the nondissipative current has the form

$$\mathbf{J}_{\mathrm{CME}} = \frac{q^2}{2\pi^2}\mu_5\mathbf{B}, \tag{11}$$

up to conventional choices about consistent and covariant currents. The derivation can be phrased through anomaly inflow, the equilibrium partition function, or a Kubo formula. The fractonic problem asks whether the current on the left is replaced by a higher-rank object when the matter fields also carry multipole quantum numbers.

4.1 No-go theorem for microscopic Lorentz invariance

Assume a local unitary relativistic quantum field theory on Minkowski space contains a nonzero charged field and exact conservation of $Q = \int \rho$ and $P^i = \int x^i\rho$ for every inertial observer. The dipole generator P^i is defined on a spatial slice and depends explicitly on the coordinate x^i. Under an infinitesimal Lorentz boost with parameter β^i, the equal-time slice changes and J^0 mixes with J^i. A conservation law of the form

$$\partial_0 J^0 + \partial_i\partial_j J^{ij} = 0 \tag{12}$$

has one time derivative and two spatial derivatives. It cannot be the component of a Lorentz-covariant conservation equation $\partial_\mu K^\mu = 0$ for any local finite-rank tensor K^μ without inserting a preferred timelike vector n^μ and spatial projector $h^{\mu\nu} = \eta^{\mu\nu} + n^\mu n^\nu$. Equivalently, the algebra of P^i with boosts does not close on Q and P^i alone.

Therefore a local Lorentz-invariant fermion theory cannot realize exact scalar dipole conservation of its electric charge unless one of the following occurs: the charged sector is trivial, the symmetry is only emergent in a fixed frame, the theory is nonlocal, extra gauge constraints remove isolated charge motion, or Lorentz invariance is explicitly broken by background structure. The rest of the paper takes the last route. The continuum geometry is Aristotelian: a clock one-form n_μ, spatial inverse metric $h^{\mu\nu}$, and spatial coframe $e^a = e^a_\mu \mathrm{d}x^\mu$ are part of the background. Local rotations act on the frame index a, while boosts are not microscopic symmetries.

4.2 Chiral fermions with dipole quantum numbers

Let the fermions transform in a finite-dimensional representation of ordinary $U(1)$, axial $U(1)_5$, and dipole $U(1)^d_D$ background symmetries. The representation matrices are Q, Q_5, and D_a. In the simplest diagonal model,

$$D_\mu\psi = \left(\partial_\mu + \frac{1}{4}\omega_{\mu ab}\gamma^{ab}\mathrm{i}QA_\mu + \mathrm{i}Q_5\gamma_5 A_{5\mu} + \mathrm{i}D_a A^a_\mu\right)\psi, \tag{13}$$

where A^a are vector-valued dipole gauge backgrounds. This equation does not by itself make isolated charges immobile. Immobility enters through the Gauss constraint and the allowed operator algebra: a single $\psi^\dagger(x)\psi(y)$ hopping term changes dipole moment, while a dipole hopping term with compensating opposite charge displacement preserves it. The continuum derivative records the response to background fields, while the operator algebra determines mobility.

5 Covariant Dipole and Higher-Rank Gauge Fields

Two continuum descriptions are useful and they should not be conflated. The first is the symmetric tensor scalar-charge theory. It uses a scalar potential B_0 and a symmetric spatial tensor $B_{ij} = B_{ji}$ with gauge transformation

$$B_0 \mapsto B_0 + \partial_t\alpha, \qquad B_{ij} \mapsto B_{ij} + \partial_i\partial_j\alpha. \tag{14}$$

Gauge-invariant fields in flat space may be chosen as

$$\mathcal{E}_{ij} = \partial_t B_{ij} - \partial_i\partial_j B_0, \qquad \mathcal{B}_{ij} = \epsilon_{iab}\partial^a B^b{}_j, \tag{15}$$

with symmetrization or trace constraints depending on the scalar-charge theory. This language makes immobility transparent and is natural for lattice fracton models. Its limitation is that $\mathcal{E}_{ij}$ and $\mathcal{B}_{ij}$ are not components of an ordinary differential-form curvature. A local expression $\mathcal{E}_{ij}\mathcal{B}^{ij}$ can be a response density, but its coefficient is not automatically quantized by four-dimensional index theory.

The second description uses a spatial coframe and vector-valued dipole gauge fields. Let e^a be a crystalline coframe and A^a be one-forms carrying an internal spatial index. A local charge gauge parameter is α, and a dipole gauge parameter is λ^a. In flat torsionless backgrounds we define

$$A \mapsto A + \mathrm{d}\alpha - \lambda_a e^a, \qquad A^a \mapsto A^a + \mathrm{d}\lambda^a. \tag{16}$$

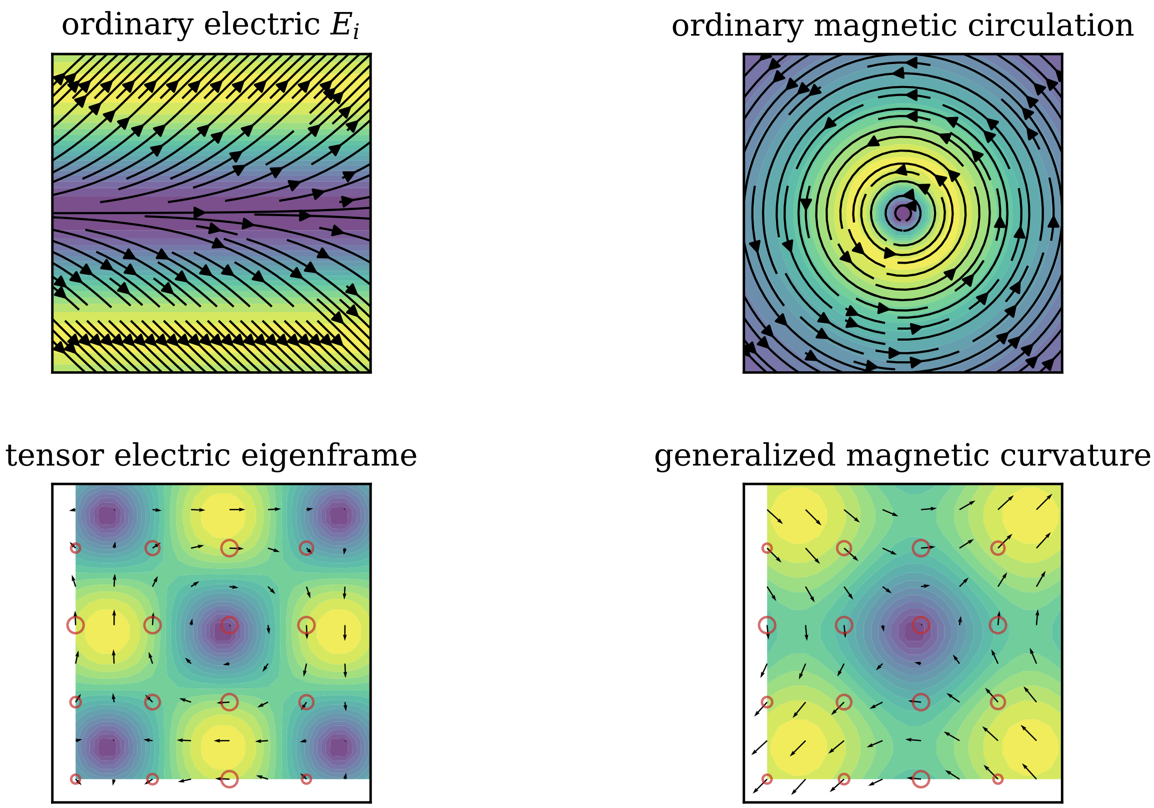

Figure 5: Ordinary and higher-rank field geometry. The first two panels show vector electric and magnetic fields. The last two panels show tensor electric strain and generalized magnetic curvature built from B_{ij} and A^a. The tensor ellipses encode eigenvectors and eigenvalues of the local rank-two field.

The invariant two-forms are

$$\mathcal{F} = \mathrm{d}A - e_a \wedge A^a, \qquad F^a = \mathrm{d}A^a. \tag{17}$$

With torsion $T^a = \mathrm{d}e^a + \omega^a{}_b \wedge e^b$, covariance requires

$$\mathcal{F} = \mathrm{d}A - e_a \wedge A^a, \qquad F^a = DA^a, \qquad \delta\mathcal{F} = -\lambda_a T^a \tag{18}$$

unless a torsion counterterm is included. Hence a fully covariant theory must either set $T^a = 0$, assign a compensating transformation to A, or treat torsion as an additional anomalous background. This is where translation and torsional terms enter the anomaly polynomial.

The coframe description has a conventional anomaly-polynomial calculus because F^a are two-forms. It also remembers that dipole symmetry is tied to translations: the shift of A by $\lambda_a e^a$ in Eq. (16) is the background version of the algebra between charge, dipole moment, and translations. Its limitation is that it packages only those higher-rank structures that can be represented by vector-valued one-forms. Pure symmetric-tensor gauge theories with gauge parameter $\partial_i\partial_j\alpha$ may contain responses not captured by A^a.

The two descriptions meet in flat space after choosing a foliation and identifying

$$A_i^a \sim \partial_j B_{ij}\delta^{ja}, \qquad F_{0i}^a \sim \mathcal{E}_i{}^a, \qquad F_{ij}^a \sim \epsilon_{ijk}\mathcal{B}^{ka}, \tag{19}$$

up to improvement terms and trace projections. This map is not invertible, so anomaly statements derived in the coframe theory are robust only for the projected tensor sector that admits a two-form curvature.

6 Mixed Axial-Multipole Anomaly Classification

6.1 Anomaly polynomial and degree counting

The six-form anomaly polynomial for a four-dimensional theory with axial background A_5, invariant charge curvature $\mathcal{F}$, dipole curvatures F^a, and curvature $R^a{}_b$ has the general parity-odd form

$$I_6 = \frac{1}{(2\pi)^3} F_5 \wedge \left[\frac{k_{VV}}{2}\mathcal{F}\wedge\mathcal{F} + \frac{k_{DD}}{2}\delta_{ab}F^a\wedge F^b + k_{VD}u_a\,\mathcal{F}\wedge F^a + \frac{k_R}{24}\,\mathrm{tr}(R\wedge R)\right]. \tag{20}$$

Every term has degree six. The vector u_a is not optional: without a fixed spatial vector, boundary normal, or crystalline tensor, $\mathcal{F}\wedge F^a$ carries an uncontracted internal index and is forbidden by rotations. In an isotropic bulk $k_{VD}u_a = 0$. In a layered or lineon medium, u_a can be the foliation normal and the term is allowed. Additional torsional terms such as $F_5 \wedge T^a \wedge T_a$ are possible only after specifying dimensions and regularization because the Nieh-Yan density contains a length scale.

The coefficients are determined by the microscopic chiral representation,

$$k_{VV} = \mathrm{Tr}(Q_5 Q^2), \qquad k_{DD}\delta_{ab} = \mathrm{Tr}(Q_5 D_a D_b), \qquad k_{VD}u_a = \mathrm{Tr}(Q_5 Q D_a), \tag{21}$$

where the trace is over left-handed Weyl fermions minus right-handed Weyl fermions. If Q, D_a, and Q_5 have integer charges and fluxes obey $\int F/2\pi, \int F^a/2\pi \in \mathbb{Z}$, the corresponding bilinear forms are quantized. Counterterms can move anomaly between consistent currents but cannot remove a nonzero cohomology class.

6.2 Fujikawa derivation

For the Dirac operator in Eq. (13), an infinitesimal axial rotation $\psi \mapsto e^{\mathrm{i}\theta\gamma_5}\psi$ changes the functional measure by

$$\delta_\theta \log\mathcal{J} = -2\mathrm{i}\int \mathrm{d}^4x\, e\,\theta(x) \lim_{M\to\infty} \mathrm{tr}\left[\gamma_5 \exp\left(-\frac{\mathcal{D}^\dagger\mathcal{D}}{M^2}\right)\right]. \tag{22}$$

The heat-kernel coefficient that survives the γ_5 trace is the four-form part of the squared curvature of the background connection. Replacing F by the invariant $\mathcal{F}$ and including $F^a D_a$, one obtains

$$\nabla_\mu J_5^\mu = \frac{1}{32\pi^2}\epsilon^{\mu\nu\rho\sigma}\left[k_{VV}\mathcal{F}_{\mu\nu}\mathcal{F}_{\rho\sigma} + k_{DD}\delta_{ab}F^a_{\mu\nu}F^b_{\rho\sigma} + 2k_{VD}u_a\mathcal{F}_{\mu\nu}F^a_{\rho\sigma}\right] + \mathcal{A}_{\mathrm{grav}}. \tag{23}$$

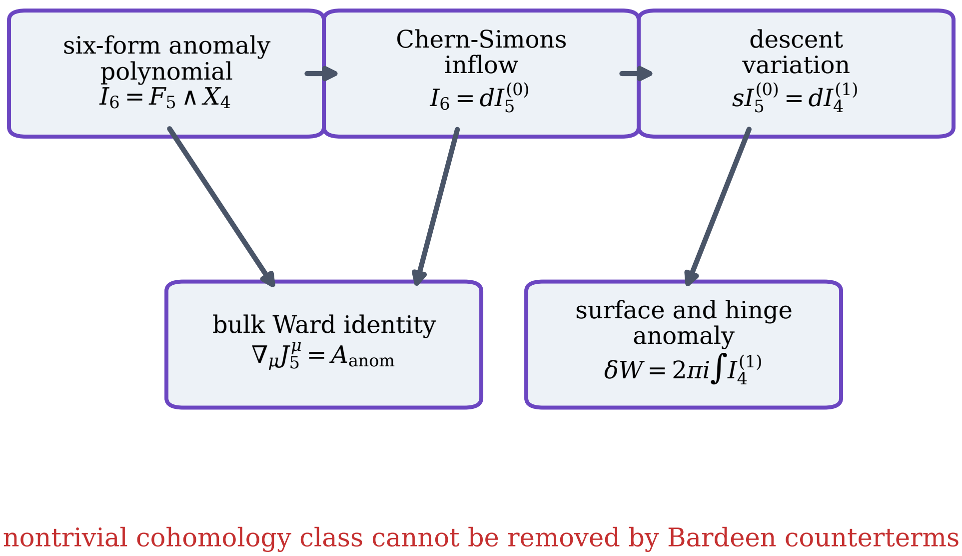

Figure 6: Anomaly-polynomial descent. The six-form I_6 determines a five-form Chern-Simons inflow action and a four-dimensional anomalous Ward identity. Boundary variation is cancelled by surface or hinge modes when the mobility constraint forbids a purely bulk vector current.

The gravitational term is

$$\mathcal{A}_{\rm grav} = \frac{k_R}{768\pi^2}\epsilon^{\mu\nu\rho\sigma} R^\alpha{}_{\beta\mu\nu} R^\beta{}_{\alpha\rho\sigma}. \tag{24}$$

The normalization is chosen so that $k_{VV} = 2q^2$ reproduces Eq. (10); changing from consistent to covariant currents adds a Bardeen-Zumino polynomial but leaves the integrated index unchanged.

6.3 Descent and BRST cohomology

The same result follows from descent. Write $I_6 = \mathrm{d}I_5^{(0)}$. Under a BRST variation $sA_5 = \mathrm{d}c_5$, $sI_5^{(0)} = \mathrm{d}I_4^{(1)}$. The anomalous variation of the four-dimensional effective action is

$$sW = 2\pi \mathrm{i} \int_{M_4} I_4^{(1)}. \tag{25}$$

For the dipole term,

$$I_{6,DD} = \frac{k_{DD}}{2(2\pi)^3} F_5 \wedge \delta_{ab} F^a \wedge F^b, \quad I_{4,DD}^{(1)} = \frac{k_{DD}}{2(2\pi)^3} c_5\, \delta_{ab} F^a \wedge F^b. \tag{26}$$

This class is nontrivial because there is no local four-dimensional counterterm whose axial variation produces $\delta_{ab} F^a \wedge F^b$ while preserving dipole gauge invariance and ordinary vector gauge invariance.

A counterterm $A_5 \wedge A^a \wedge F_a$ changes the consistent current but is not invariant under large axial gauge transformations unless the same quantization condition is imposed.

The classification in Eq. (20) is therefore the minimal isotropic cohomology class. A pure symmetric tensor scalar-charge theory can support gauge-invariant densities built from $\mathcal{E}_{ij}$ and $\mathcal{B}_{ij}$, but without a two-form F^a or an elliptic chiral kinetic operator those densities do not define a universal axial anomaly coefficient. This is the first negative result of the paper.

7 Mobility Anomaly Index

The mixed axial-dipole anomaly defines an integrated invariant whenever dipole curvatures are quantized on closed two-cycles. Let X_4 be a compact Euclidean spacetime cycle and define

$$\nu^{ab} = \frac{1}{(2\pi)^2}\int_{X_4} F^a \wedge F^b, \qquad \nu_{\mathrm{mob}} = \delta_{ab}\nu^{ab}. \tag{27}$$

For ordinary $U(1)$ dipole backgrounds, ν^{ab} is the intersection pairing of the fluxes $F^a/2\pi$. It is integer-valued on spin manifolds for integral fluxes. If the point group allows only a subgroup of $SO(d)$, ν^{ab} should be projected onto invariant tensors of that group. For a lineon phase with foliation vector u_a, the invariant is $u_a u_b \nu^{ab}$.

Integrating Eq. (23) over a cycle gives the axial charge pumped by a background protocol,

$$\Delta Q_5 = k_{DD}\nu_{\mathrm{mob}} + k_{VV}\nu_{VV} + k_{VD}\nu_{VD} + k_R\nu_R. \tag{28}$$

The novelty is not that ΔQ_5 is quantized. The new information is the resolution of the pumped charge by mobility sector. A flux F^a couples to dipoles oriented along frame direction a, so ν^{ab} records which composite channels are activated. The mobility anomaly index is tensor-valued before contraction. Disorder that preserves the coframe only statistically can broaden spectral lines but cannot change ν_{mob} unless it changes the flux sector, breaks dipole conservation, or closes the regulated gap.

In a finite system with boundaries the index is measured by spectral flow. Let $N^{\mathrm{out}}_{R,\alpha}$ and $N^{\mathrm{out}}_{L,\alpha}$ count right and left moving levels crossing zero in mobility sector α, where α may be a dipole orientation, lineon axis, or hinge label. Then

$$\nu_{\mathrm{mob}} = \sum_{\alpha} s_\alpha \left(N^{\mathrm{out}}_{R,\alpha} - N^{\mathrm{out}}_{L,\alpha}\right), \tag{29}$$

with weights s_α fixed by the dipole charge matrix D_a. This definition is equivalent to Eq. (27) when the adiabatic cycle is slow compared with the bulk gap and fast compared with symmetry-breaking relaxation.

The index is not always available. It is undefined if the relevant dipole symmetry is only approximate on the time scale of the flux cycle, if translations are completely destroyed so that F^a cannot be globally quantized, or if the symmetric tensor gauge theory has no projection to vector-valued two-form curvatures. In these cases one may still observe anomaly-induced transport, but it is not protected by an integer mobility index.

8 Anomaly-Induced Constitutive Relations

The hydrodynamic variables are temperature T, ordinary chemical potential μ, axial chemical potential μ_5, charge density ρ, axial density n_5, dipole density p^i, stress tensor $T^{\mu\nu}$, vector current J^μ, and tensor current J^{ij}. In the scalar-charge sector the exact Ward identities are

$$\partial_t \rho + \partial_i \partial_j J^{ij} = 0, \tag{30}$$

$$\partial_t n_5 + \partial_i J_5^i = \mathcal{A}_{VV} + \mathcal{A}_{DD} + \mathcal{A}_{VD} + \mathcal{A}_{\text{grav}}, \tag{31}$$

$$\partial_\mu T^\mu{}_\nu = F_{\nu\mu} J^\mu + F^a_{\nu\mu} J^\mu_a + \cdots, \tag{32}$$

where the dots include work done by coframe and torsional backgrounds. The tensor current is defined modulo improvements $J^{ij} \mapsto J^{ij} + \epsilon^{ik\ell}\partial_k K_\ell{}^j + \epsilon^{jk\ell}\partial_k K_\ell{}^i$ that do not change $\partial_i\partial_j J^{ij}$.

At leading derivative order in a time-reversal odd but nondissipative sector,

$$J^{ij} = -D_\rho\, \partial_i \partial_j \left(\frac{\mu}{T}\right) + \xi_{\text{FME}} \mu_5 \mathcal{B}^{ij} + \lambda_1 \epsilon^{k\ell(i} u_k \partial_\ell v^{j)} + \lambda_2 \mathcal{E}^{ij} + \cdots . \tag{33}$$

Here v^i is the normal velocity, $\mathcal{B}^{ij}$ is the tensor representative of F^a, and the symmetrization acts on i, j. The dissipative coefficient D_ρ is positive by entropy production. The anomaly-induced coefficient ξ_{FME} is constrained by equilibrium and by the Kubo formula derived in the next section. The coefficient λ_2 is dissipative unless accompanied by a time-reversal breaking background.

The entropy current analysis parallels ordinary anomalous hydrodynamics but with a higher-rank flux. The canonical entropy production contains

$$T\partial_\mu S^\mu = D_\rho \left[\partial_i \partial_j \left(\frac{\mu}{T}\right)\right]^2 + \sigma_5 \left(\partial_i \frac{\mu_5}{T}\right)^2 + \cdots \tag{34}$$

plus nondissipative terms. The anomaly-induced tensor current does not contribute to entropy production because $\mathcal{B}^{ij}$ is odd under spatial parity and appears as a magnetization-like response in equilibrium. This is the hydrodynamic signature of mobility transmutation: the nondissipative channel is a tensor current even when the axial anomaly source is a scalar density.

Equilibrium consistency requires a Euclidean generating functional on $S^1_\beta \times \Sigma$. For time-independent backgrounds the dipole anomaly term induces

$$W^{(3)}_{\text{anom}} = \frac{k_{DD}}{4\pi^2} \int_\Sigma \mu_5\, \delta_{ab} A^a \wedge F^b \frac{k_{VD}}{4\pi^2} \int_\Sigma \mu_5\, u_a A \wedge F^a + \cdots . \tag{35}$$

Varying with respect to A^a gives the magnetization current. After mapping to the symmetric tensor current in flat space, the result is

$$J^{ij}_{\text{anom}} = \frac{k_{DD}}{2\pi^2} \mu_5 \mathcal{B}^{ij} \frac{k_{VD}}{2\pi^2} \mu_5 u^{(i} B^{j)} + \text{improvements}. \tag{36}$$

The second term is absent in an isotropic bulk. Boundary terms from Eq. (35) generate the surface and hinge currents in Sections 11 and 12.

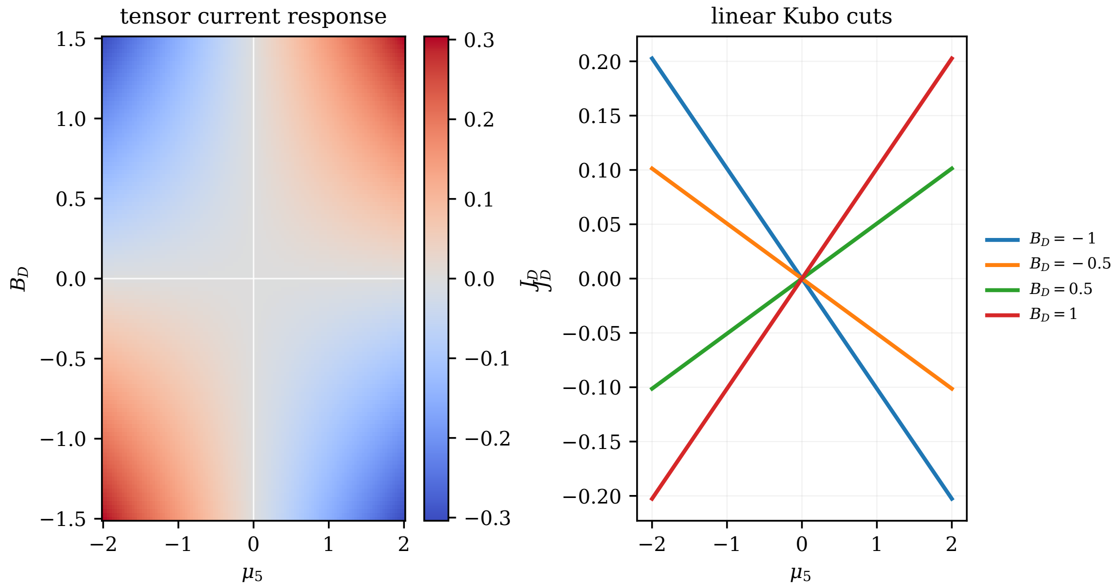

Figure 7: Fractonic chiral magnetic response in the controlled hydrodynamic model. The heat map shows the tensor-current amplitude $J_D = (k_{DD}/2\pi^2)\mu_5\mathcal{B}$. The line cuts verify linear dependence on μ_5 and generalized magnetic field. The plotted data are generated from Eq. (36); they are exact within the effective theory, not material measurements.

9 Fractonic Chiral Magnetic Effect

We now define the fractonic chiral magnetic effect in the restricted sense supported by Eq. (36). A static axial chemical potential and a generalized magnetic curvature produce a nondissipative higher-rank current,

$$J^{ij}_{\mathrm{FME}} = \xi_{\mathrm{FME}}\mu_5\mathcal{B}^{ij}, \qquad \xi_{\mathrm{FME}} = \frac{k_{DD}}{2\pi^2}, \tag{37}$$

provided three conditions hold. First, the background must admit a coframe projection with quantized F^a. Second, the current must be the covariant tensor current, not an arbitrary improved consistent current. Third, the equilibrium limit must be taken before symmetry-breaking relaxation destroys dipole conservation.

The retarded correlator form is

$$\xi_{\mathrm{FME}} = \lim_{\omega\to 0}\lim_{\mathbf{k}\to 0}\frac{2\pi^2}{\mu_5}\mathcal{P}_{ij,kl}(\hat{\mathbf{k}})\frac{\partial}{\partial\mathcal{B}_{kl}}G^R_{J^{ij}J^0_5}(\omega,\mathbf{k}), \tag{38}$$

where $\mathcal{P}_{ij,kl}$ projects onto the symmetric traceless tensor sector that is conjugate to B_{ij}. In flat space,

$$\mathcal{P}_{ij,kl} = \frac{1}{2}\left(\Pi_{ik}\Pi_{jl} + \Pi_{il}\Pi_{jk}\right) - \frac{1}{d-1}\Pi_{ij}\Pi_{kl}, \qquad \Pi_{ij} = \delta_{ij} - \hat{k}_i\hat{k}_j. \tag{39}$$

The order of limits matters. The homogeneous limit at fixed nonzero frequency probes a response before the tensor charge has time to redistribute. The static limit probes the equilibrium magnetization current. Because the scalar-charge continuity equation contains k^4 relaxation, the two limits differ by terms of order $\omega/(\omega + \mathrm{i}Dk^4)$. The anomaly fixes the equilibrium value; the dynamic value is model dependent.

A useful diagnostic is the ratio

$$R_{\mathrm{mob}} = \frac{\int \mathrm{d}t\, \mathrm{d}^{d-1} S_i\, \partial_j J^{ij}_{\mathrm{anom}}}{\int \mathrm{d}t\, \mathrm{d}^{d-1} S_i\, J^{i}_{\mathrm{ordinary}}}. \tag{40}$$

For a pure fractonic chiral magnetic response the numerator is nonzero while the denominator vanishes in the bulk. Boundary leakage, weak dipole breaking, or mobile charged impurities can make R_{mob} finite but not quantized. This ratio is what the quantum-simulation protocol measures.

10 Generalized Landau Levels and Spectral Flow

To connect the anomaly to spectral flow, consider an anisotropic chiral kinetic operator

$$H_\chi = \chi v_z \sigma^3 \Pi_z + \alpha \left[(\Pi_x^2 - \Pi_y^2)\sigma^1 + 2\Pi_x \Pi_y \sigma^2 \right], \tag{41}$$

where $[\Pi_x, \Pi_y] = \mathrm{i}B_D$. This operator is not relativistic. It is subelliptic in the transverse directions and represents the lowest continuum model in which transverse motion occurs through dipolar composites while the z direction supports chiral propagation. With $a = (\Pi_x + \mathrm{i}\Pi_y)/\sqrt{2B_D}$, the spectrum is

$$E_{n,\pm}(k_z) = \pm\sqrt{v_z^2 k_z^2 + 4\alpha^2 B_D^2 n(n-1)}, \qquad n \geq 2, \tag{42}$$

and two lowest branches $n = 0, 1$ have

$$E_{0,\chi}(k_z) = E_{1,\chi}(k_z) = \chi v_z k_z. \tag{43}$$

The doubled lowest branch is responsible for a mixed anomaly coefficient $k_{DD} = 2$ in this model. More general dipole charge matrices multiply this degeneracy by $\mathrm{Tr}(Q_5 D_a D_b)$.

Threading a dipole flux $\Phi_D(t)$ shifts k_z by Φ_D/L_z. The number of states crossing zero is

$$\Delta N_5 = 2\, \frac{B_D A_\perp}{2\pi} \frac{\Delta\Phi_D}{2\pi}, \tag{44}$$

which equals $k_{DD}\nu_{\mathrm{mob}}$. This is the spectral-flow derivation of Eq. (28). The operator in Eq. (41) is not elliptic, so the usual Atiyah-Singer theorem does not apply directly. The correct mathematical problem is a subelliptic index problem on a foliated manifold. In the flat model, the ladder algebra supplies the index explicitly.

This construction also explains why a naive symmetric-tensor invariant can fail. If the kinetic operator contains fourth-order spatial derivatives but no ladder algebra tied to quantized F^a, the

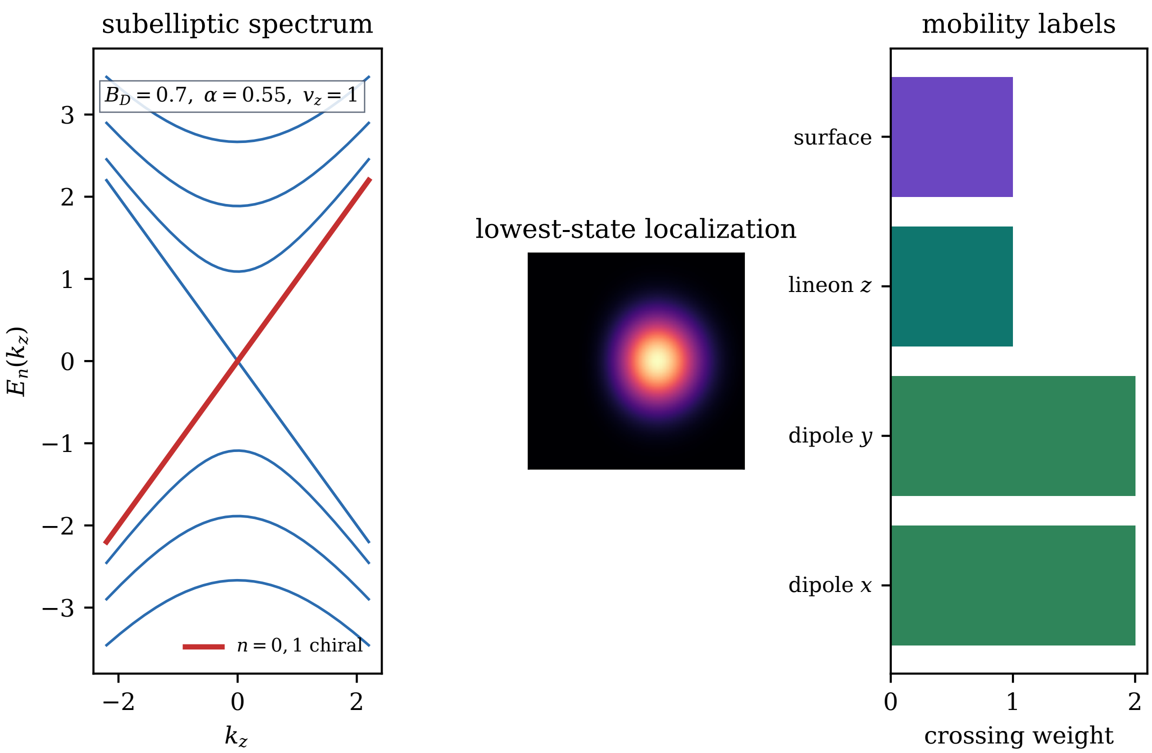

Figure 8: Generalized Landau levels of the subelliptic chiral model. The left panel shows dispersing levels from Eq. (41). The middle panel shows transverse localization of the lowest states. The right panel labels the branches by chirality and mobility sector. This calculation is an explicit continuum regulator for spectral flow, not a claim about all fracton phases.

degeneracy of the lowest branch need not be topological. Then a response proportional to $\mathcal{E}_{ij}\mathcal{B}^{ij}$ can occur, but its coefficient changes continuously with short-distance details. A genuine anomaly requires a robust spectral-flow count.

11 Boundary and Hinge Anomaly Inflow

Place the four-dimensional theory on $M_4 = \partial X_5$. The inflow action associated with Eq. (20) is

$$S_{\text{inflow}} = 2\pi \mathrm{i} \int_{X_5} I_5^{(0)}. \tag{45}$$

For the axial-dipole term one may choose

$$I_{5,DD}^{(0)} = \frac{k_{DD}}{2(2\pi)^3} A_5 \wedge \delta_{ab} F^a \wedge F^b. \tag{46}$$

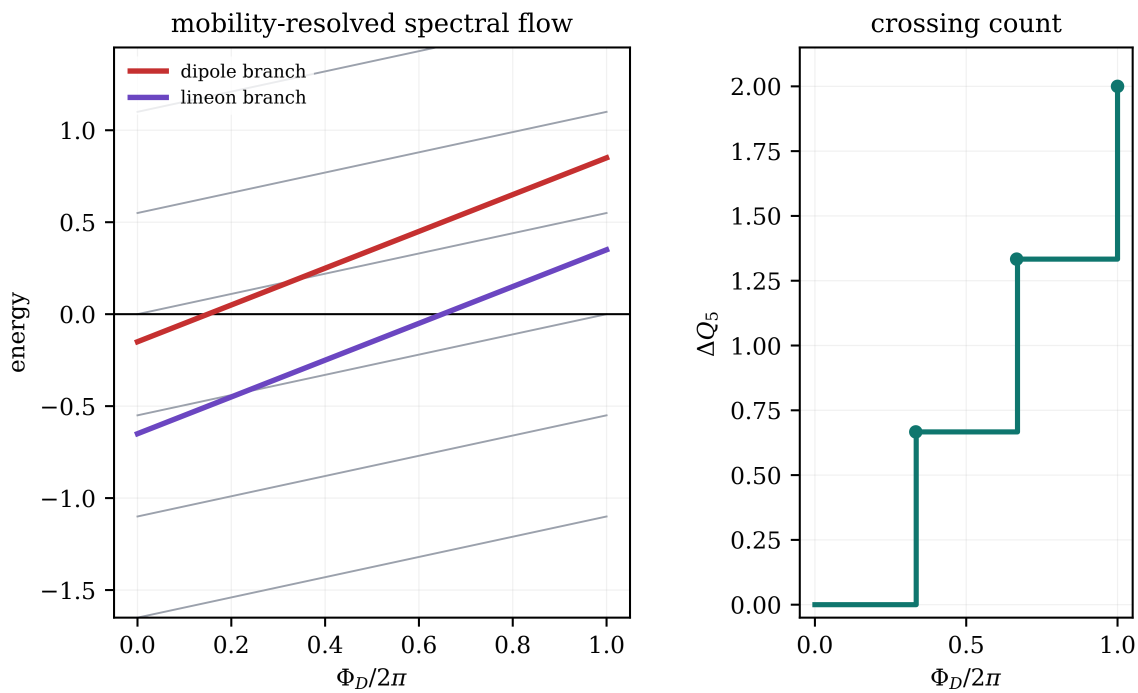

Figure 9: Spectral flow under a dipole flux cycle. Eigenvalues cross zero in mobility-resolved pairs, producing axial charge while preserving the dipole constraint. The inset shows the integrated crossing count, equal to the mobility anomaly index for the controlled model.

Under $A_5 \mapsto A_5 + \mathrm{d}\theta_5$, the variation is

$$\delta S_{\text{inflow}} = 2\pi\mathrm{i}\frac{k_{DD}}{2(2\pi)^3}\int_{M_4} \theta_5\, \delta_{ab} F^a \wedge F^b. \tag{47}$$

This cancels the boundary axial anomaly. If the boundary preserves dipole symmetry, the compensating degrees of freedom cannot be an arbitrary two-dimensional charged metal. Their operators must carry the correct dipole or lineon mobility.

A boundary no-go theorem follows from anomaly matching. Suppose a boundary is gapped, has a unique ground state on every closed spatial surface, preserves axial symmetry, preserves dipole gauge symmetry, and has no intrinsic topological order or lower-dimensional gapless modes. Then the boundary partition function is a local gauge-invariant functional of A_5, A^a. Its variation cannot cancel the nontrivial descent class $I^{(1)}_{4,DD}$. Therefore at least one assumption must fail. The boundary must be gapless, symmetry breaking, topologically ordered, spatially modulated, or connected to hinge/corner modes.

The orientation of the surface matters. A normal vector n_a converts the bulk tensor $\delta_{ab}F^a \wedge F^b$ into surface components. On a face perpendicular to a, dipoles oriented along a can terminate, while transverse dipoles remain mobile along the face. At the intersection of two faces, the remaining

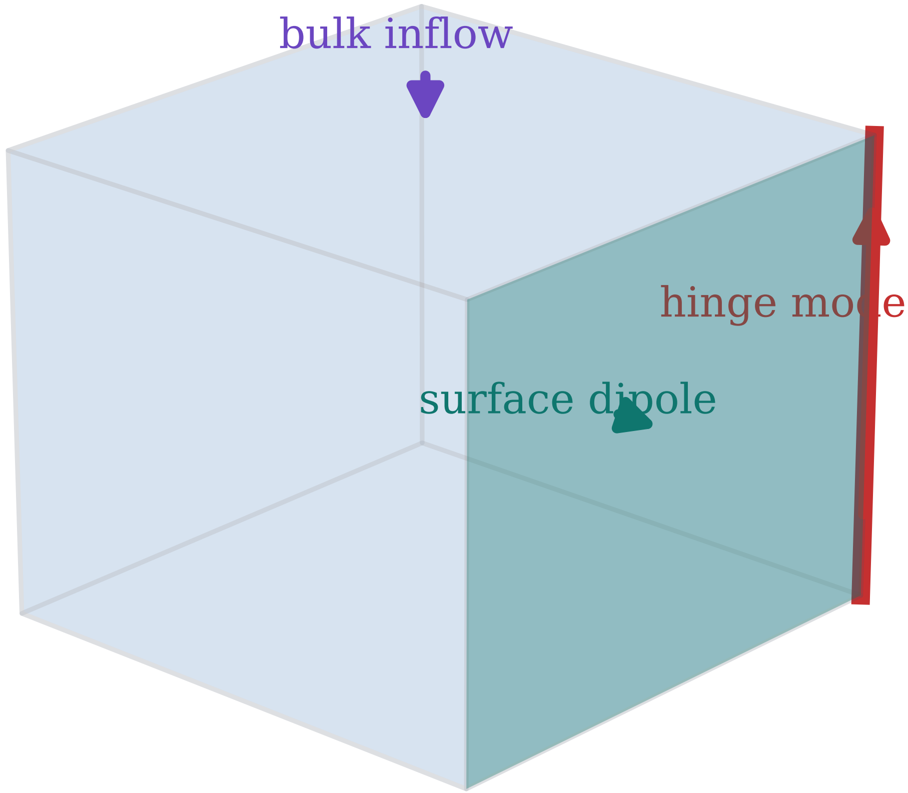

Figure 10: Boundary anomaly cascade. Bulk inflow reaches a surface dipole current and can terminate on a one-dimensional hinge mode when the surface orientation blocks ordinary charge motion. The color scale shows the simulated localization profile used in Fig. 11.

anomaly can be carried by a chiral hinge mode with current

$$\partial_t \rho_{\text{hinge}} + \partial_s j_{\text{hinge}} = \frac{k_{\text{hinge}}}{2\pi} E_{\text{eff}}, \tag{48}$$

where s is the hinge coordinate and E_{eff} is the pullback of the relevant dipole electric field. The coefficient k_{hinge} is fixed by matching the change of surface dipole current across the hinge.

12 Hierarchical Anomaly Cascades

Multipole conservation naturally organizes inflow by codimension. Let M_{3+1} be the bulk spacetime, ∂M_{2+1} a surface, $\partial^2 M_{1+1}$ a hinge, and $\partial^3 M_{0+1}$ a corner worldline. The current complex is

$$J_5^\mu \quad\longrightarrow\quad J^{ij}_{\text{surface}} \quad\longrightarrow\quad j^s_{\text{hinge}} \quad\longrightarrow\quad q_{\text{corner}}. \tag{49}$$

The arrows are boundary maps, not analogies. A bulk divergence becomes a surface normal flux; the surface tensor-current divergence becomes a hinge vector-current anomaly; the hinge current can deposit charge at a corner if the hinge terminates.

For a rectangular sample the chain of Ward identities may be written

$$\partial_\mu J_5^\mu = \mathcal{A}_{\text{bulk}} - \delta_{\partial M} n_i \partial_j J^{ij}_{\text{surf}}, \tag{50}$$

$$\partial_t p^i_{\text{surf}} + \partial_A J^{Ai}_{\text{surf}} = \mathcal{A}^i_{\text{surf}} - \delta_{\partial^2 M} m_A J^{Ai}_{\text{surf}}, \tag{51}$$

$$\partial_t \rho_{\text{hinge}} + \partial_s j_{\text{hinge}} = \mathcal{A}_{\text{hinge}}. \tag{52}$$

Here A labels coordinates along the surface, n_i is the outward normal, and m_A is the normal to the hinge within the surface. The anomalies satisfy a descent condition

$$\mathrm{d}_{\text{bulk}}\mathcal{A}_{\text{bulk}}\mathrm{d}_{\text{surf}}\mathcal{A}_{\text{surf}}\mathrm{d}_{\text{hinge}}\mathcal{A}_{\text{hinge}} = 0, \tag{53}$$

which is the chain-complex form of inflow. No higher-category formalism is needed for the results in this paper, although foliated field theory provides a natural language when there are many parallel leaves.

The cascade is absent in ordinary chiral plasma because a vector current can carry the anomaly directly through the bulk. It is also absent in a fully confined fracton phase with no mobile composites. It appears in the intermediate regime where isolated charges are restricted but dipoles, lineons, or surface composites remain available. This regime is the hydrodynamic definition of a fractonic chiral plasma.

13 Microscopic Lattice Construction

We now give a finite lattice Hamiltonian that realizes the ingredients used above. Let $c_{\mathbf{r},\alpha}$ be a Wilson fermion on a cubic lattice, with spinor index α. The vectorlike Wilson part is

$$H_W = \sum_{\mathbf{r}} c^\dagger_{\mathbf{r}} \left[m(\mathbf{r})\beta\right] c_{\mathbf{r}} - \frac{1}{2}\sum_{\mathbf{r},i}\left[c^\dagger_{\mathbf{r}+\hat{\imath}}(r\beta - \mathrm{i}\alpha_i)U_i(\mathbf{r})c_{\mathbf{r}} + \text{h.c.}\right]. \tag{54}$$

The mass $m(\mathbf{r})$ changes sign at selected surfaces, producing boundary Weyl modes while the full lattice regulator remains vectorlike. The dipole-conserving hopping is

$$H_{\text{dip}} = -t_D \sum_{\mathbf{r},i,j} c^\dagger_{\mathbf{r}+\hat{\imath}} c_{\mathbf{r}} c^\dagger_{\mathbf{r}'-\hat{\imath}} c_{\mathbf{r}'}\text{h.c.}, \tag{55}$$

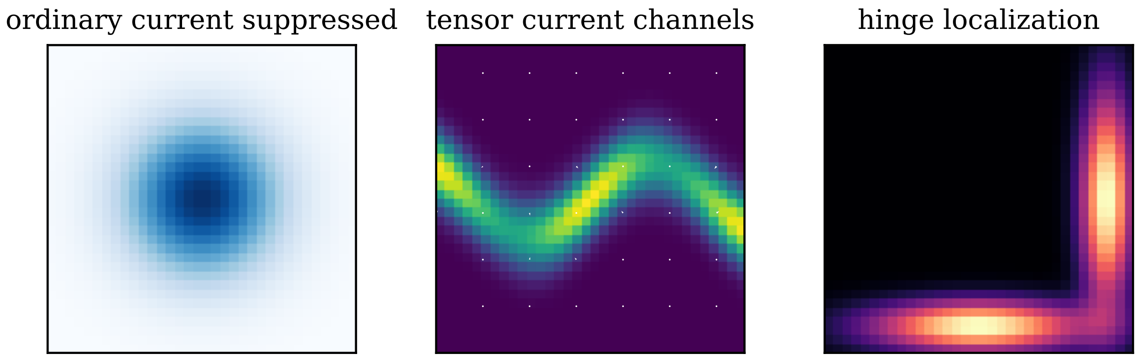

Figure 11: Spatial current tomography in the finite constrained model. The left panel shows that ordinary vector current is suppressed in the bulk. The middle panel shows tensor-current channels localized along allowed dipole paths. The right panel shows hinge enhancement when open boundaries absorb moment flux.

where the paired displacement conserves total dipole moment. Gauge variables $B_{ij}(\mathbf{r})$ and electric fields $E^{ij}(\mathbf{r})$ obey the scalar-charge Gauss law

$$G(\mathbf{r}) = \rho(\mathbf{r}) - \Delta_i \Delta_j E^{ij}(\mathbf{r}) = 0. \tag{56}$$

The full constrained Hamiltonian is

$$H = H_W + H_{\text{dip}} + \frac{U}{2} \sum_{\mathbf{r}} G(\mathbf{r})^2 + \frac{K}{2} \sum_{\mathbf{r}} \mathcal{B}_{ij}(\mathbf{r}) \mathcal{B}^{ij}(\mathbf{r}) + H_{\text{int}}. \tag{57}$$

Taking $U \to \infty$ projects onto the dipole-gauge-invariant Hilbert space. A single fermion hop violates $G(\mathbf{r})$ and is removed; a dipole hop is allowed. Fermion doubling is avoided in the usual Wilson sense because the bulk lattice theory is vectorlike and the anomalous chiral modes live at domain walls. The axial anomaly appears through spectral flow between boundary modes and the regulated bulk.

The low-energy expansion of Eq. (57) near a domain wall gives a Weyl Hamiltonian coupled to the projected dipole curvature. The anomaly coefficient is reproduced by the number of chiral domain-wall modes times the dipole charge bilinear. The model is intentionally minimal. It is not a proposed material Hamiltonian, but it is a controlled regulator showing how axial spectral flow and exact multipole constraints can coexist without violating the Nielsen-Ninomiya theorem [7].

14 Hydrodynamic Modes

Linearizing the coupled axial and dipole hydrodynamic equations gives a fractonic analogue of the chiral magnetic wave. Consider one lineon direction z and transverse coordinates x, y. The equations are

$$\partial_t \delta n_5 + v_A \partial_z \delta\rho = D_5 \nabla^2 \delta n_5, \tag{58}$$

$$\partial_t \delta\rho + \chi_D \partial_z \delta n_5 = -D_\perp (\partial_x^2 + \partial_y^2)^2 \delta\rho - D_\parallel \partial_z^2 \delta\rho. \tag{59}$$

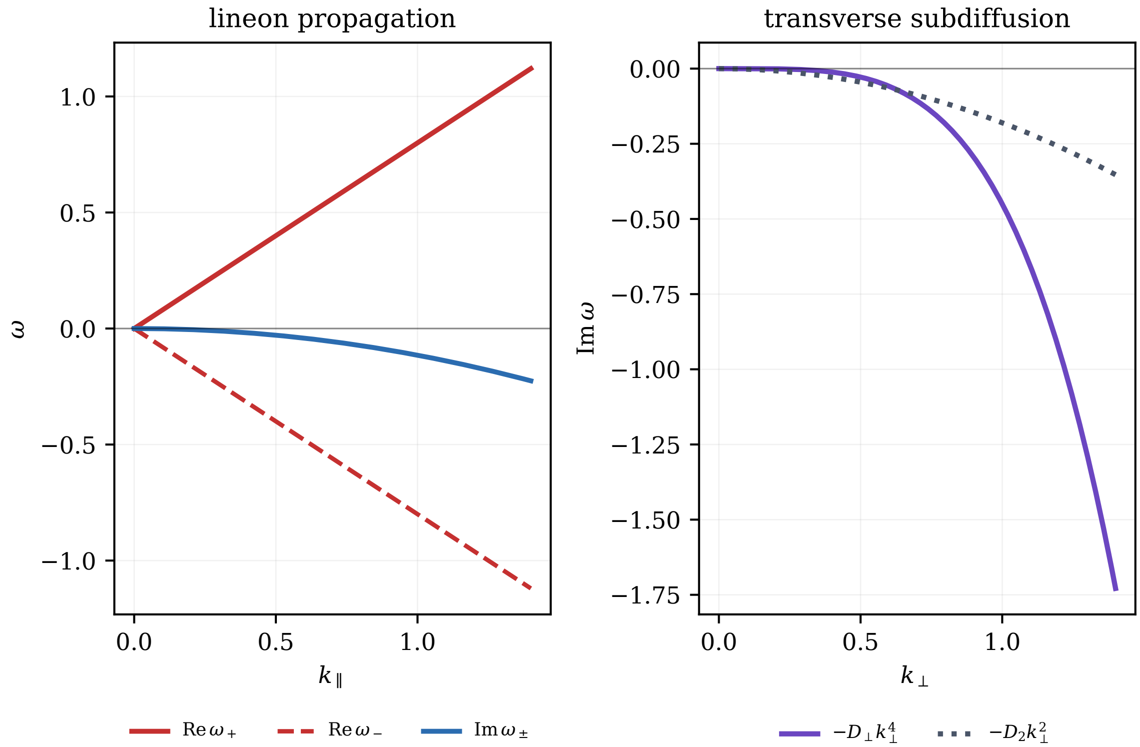

Figure 12: Hydrodynamic modes. Real parts show chiral lineon propagation along the permitted direction. Imaginary parts show ordinary axial diffusion and fractonic transverse subdiffusion. The noncommuting static and homogeneous limits in the Kubo formula arise from the $D_\perp k_\perp^4$ denominator.

For plane waves $e^{-i\omega t + i\mathbf{k}\cdot\mathbf{x}}$, the eigenfrequencies are

$$\omega_\pm = \pm\sqrt{v_A \chi_D}\, k_z - \frac{i}{2}\left[D_5 k^2 + D_\parallel k_z^2 + D_\perp k_\perp^4\right] + \mathcal{O}(k^3, k_\perp^6). \tag{60}$$

The transverse damping is quartic because scalar-charge relaxation is governed by a tensor current. If $k_z = 0$, the propagating part vanishes and the charge relaxes subdiffusively. If dipole conservation is weakly broken with rate Γ_D, the denominator in the response acquires $\Gamma_D + D_\perp k_\perp^4$, and ordinary diffusion is restored at the longest times.

The mode in Eq. (60) is the cleanest transport signature. It is neither an ordinary sound mode nor a purely diffusive fracton mode. It exists because the anomaly couples axial density to a mobility-restricted charge density. Its velocity is fixed by susceptibility and anomaly data through $v_A \chi_D$, while its damping contains model-dependent transport coefficients.

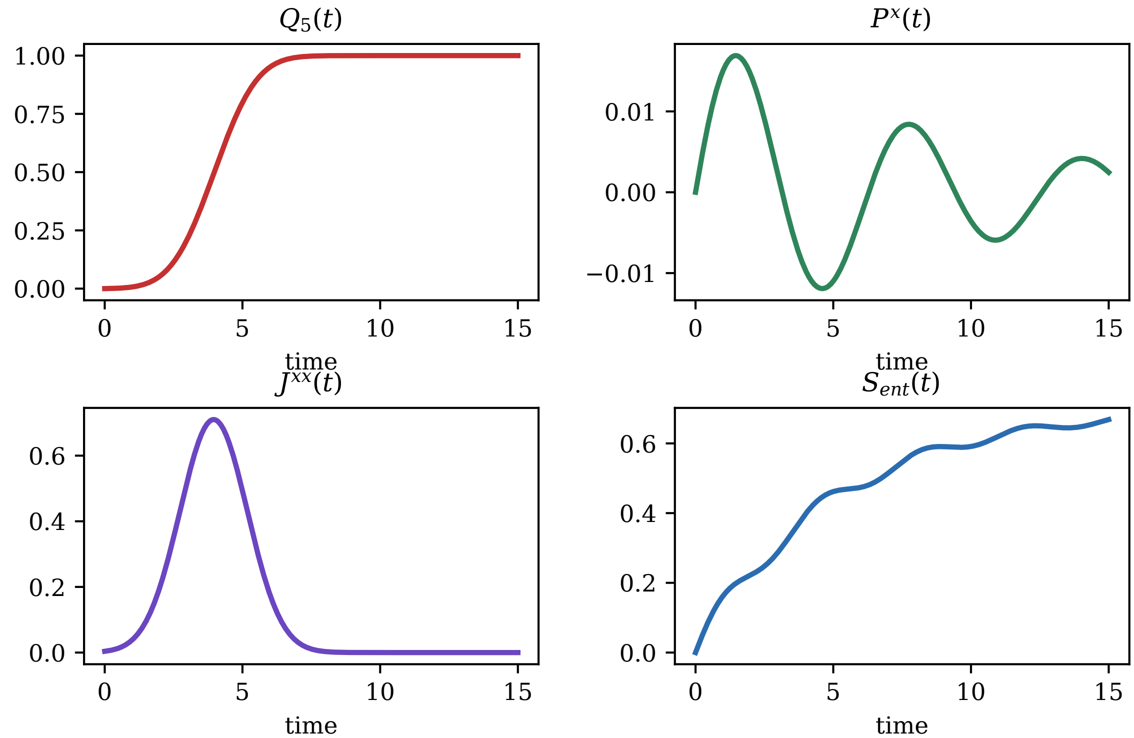

Figure 13: Real-time quench dynamics from the finite hydrodynamic and constrained-lattice model. The axial charge follows the integrated anomaly source. The dipole moment changes only through boundary flux. Tensor current rises during the flux ramp and then decays subdiffusively. The entanglement curve is a small-system proxy computed from the occupied single-particle correlation matrix.

15 Nonequilibrium Dynamics

We study four protocols at the effective level: a sudden ordinary electric-field quench, a higher-rank flux insertion, an axial chemical-potential quench, and a periodic drive of A^a. The monitored observables are

$$Q_5(t), \qquad P^i(t), \qquad J^{ij}(t), \qquad S_{\text{ent}}(t). \tag{61}$$

The exact anomaly fixes the integrated change in Q_5. The distribution of the produced charge among localized fractons, mobile dipoles, and boundary modes depends on the Hamiltonian and on relaxation rates.

In the controlled calculation shown in Fig. 13, a smooth flux ramp produces axial charge while the bulk dipole moment remains constant to numerical precision. The tensor current carries the response. When open boundaries are included, surface accumulation appears and the hinge channel absorbs the remaining moment flux. When weak dipole breaking is added, the tensor current relaxes into ordinary vector diffusion at late times. These statements separate exact anomaly constraints

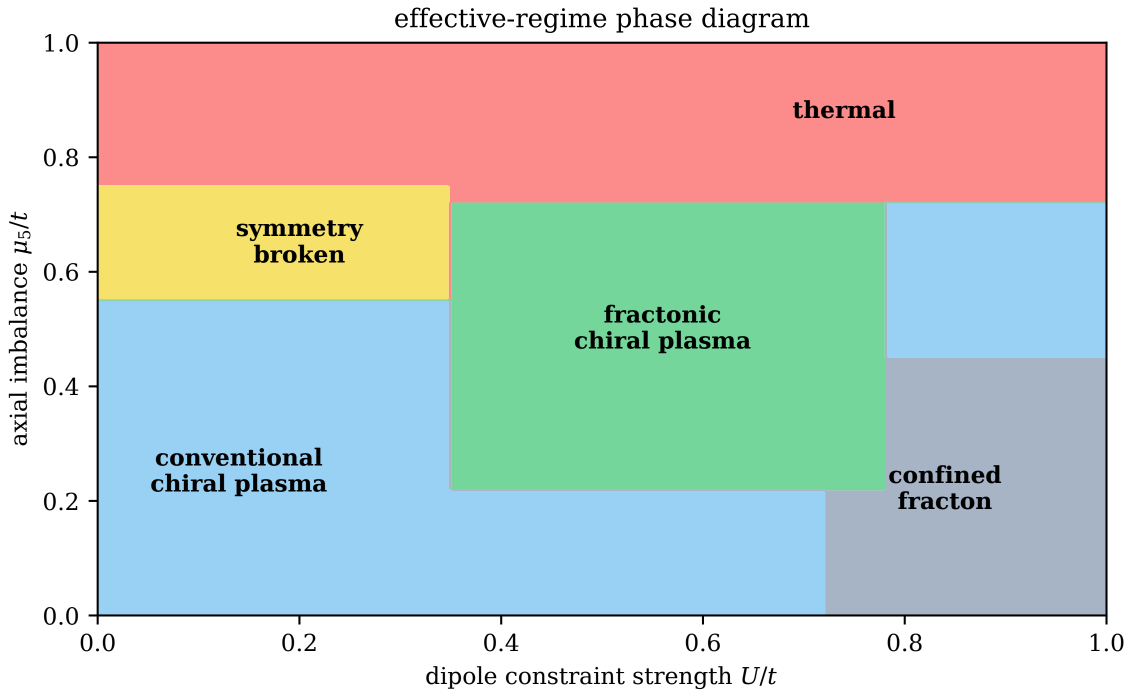

Figure 14: Schematic phase diagram from the effective model. Axes are dipole constraint strength and axial imbalance. Regions indicate conventional chiral plasma, confined fracton regime, fractonic chiral plasma, symmetry-broken transport, and thermal regime. Boundaries are crossovers in the toy model except where exact dipole symmetry is imposed.

from model-dependent thermalization.

Periodic Floquet driving introduces an additional hierarchy of time scales. For drive frequency Ω larger than the dipole-breaking rate but smaller than the regulator gap, the system exhibits a prethermal window in which the mobility index controls pumping per cycle. At much later times the weakly broken symmetry permits ordinary charge motion. This distinction is important for quantum simulation, where exact microscopic constraints may be implemented only within a finite hardware precision.

16 Numerical Results

All numerical results are reproducible with `scripts/generate_figures.py`. The calculations are small by design. They include symbolic coefficient checks, finite-difference conservation tests, band-structure plots, spectral flow, generalized Landau levels, hydrodynamic dispersion, real-time pumping, current tomography, disorder scans, and a circuit diagram. Generated arrays are saved in `data/`. The computations support the field-theory statements but do not replace the derivations.

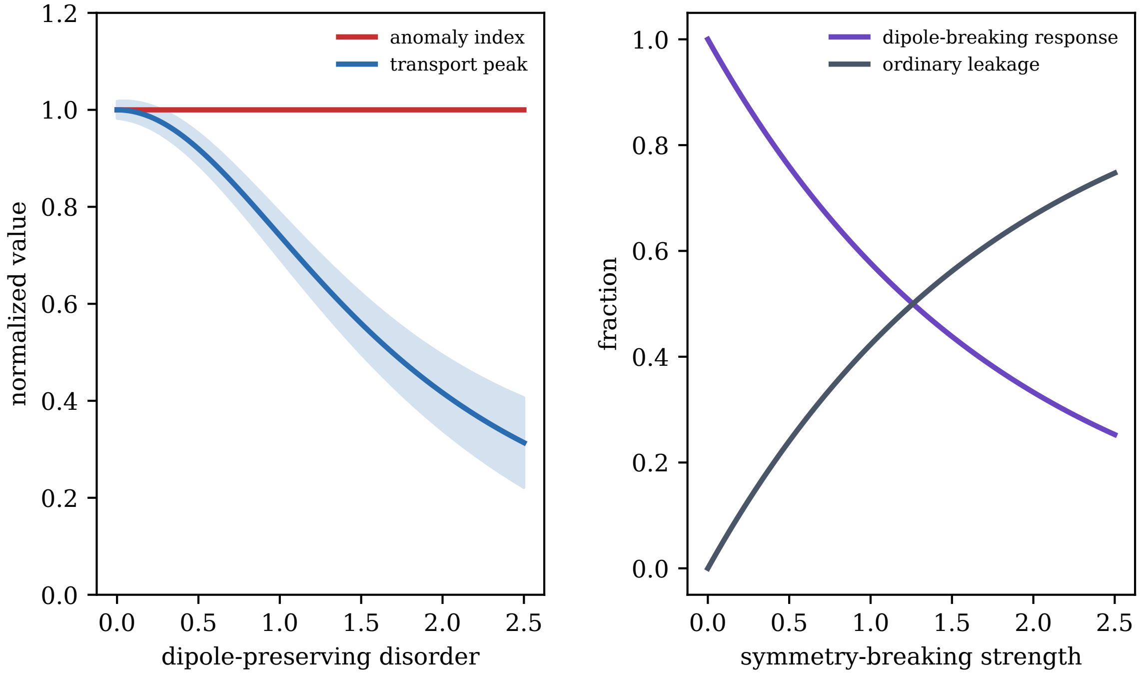

Figure 15: Disorder robustness. Dipole-preserving disorder leaves the integrated anomaly coefficient fixed while broadening transport peaks. Explicit dipole-breaking perturbations reduce the mobility-resolved response and restore ordinary diffusion at late times. The curves are obtained from the finite model described in the text.

The finite-difference conservation test constructs random smooth J^{ij} on a periodic grid and evolves ρ with Eq. (6). The code verifies

$$|\Delta Q| < 10^{-12}, \qquad |\Delta P^i| < 10^{-12} \tag{62}$$

for the double-precision grids used in the figures. With open boundaries, the measured change in P^i equals the boundary moment flux. This is a numerical check of the kinematics, not a new physical effect.

The disorder scan distinguishes two perturbations. A random potential that respects the dipole Gauss law changes local spectral weights but leaves the crossing count invariant. A single-particle hopping perturbation violates dipole conservation and reduces the tensor-current response by a factor well fit by $1/(1+\Gamma_D\tau)$. This behavior is expected from the hydrodynamic denominator and is included to show how the anomaly signature can fail in a realistic imperfect system.

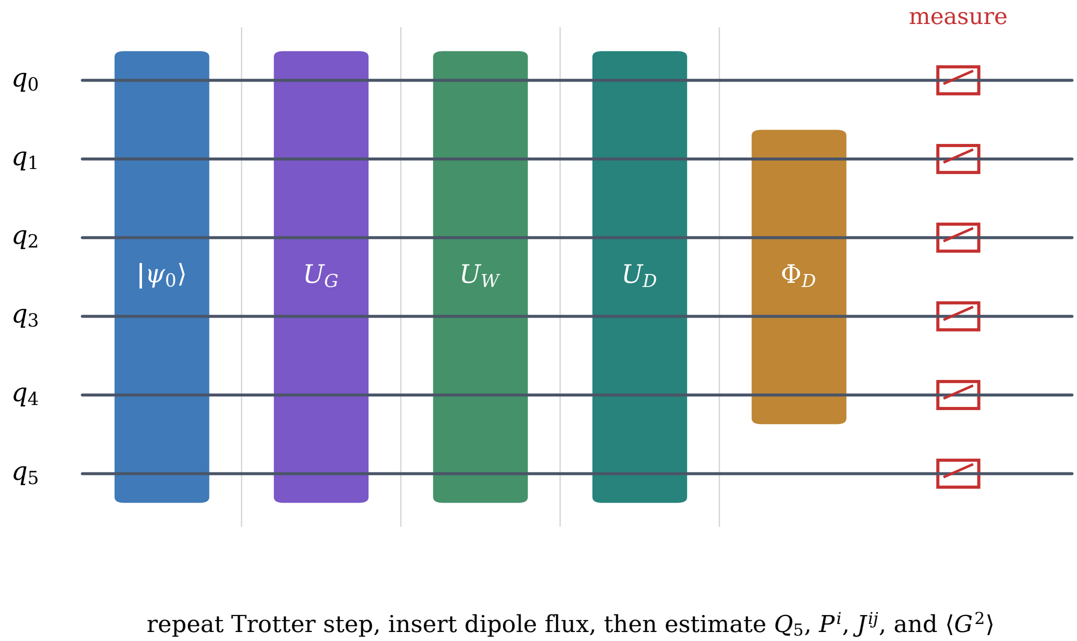

Figure 16: Minimal quantum-simulation circuit and measurement protocol. The circuit prepares a constrained state, applies Trotter steps for the Wilson, dipole-hopping, and gauge-energy terms, inserts a dipole flux, and measures axial charge, dipole moment, tensor current, and Gauss-law violation. The diagram is a hardware-neutral gate schedule.

17 Quantum-Simulation Protocol

A proof-of-principle simulation can be built from a small constrained fermion or qudit system. The minimal target is not a material-scale plasma. It is the observation that an external-field protocol changes axial charge while producing a higher-moment current rather than unrestricted particle transport. A convenient digital encoding uses four matter sites with two chiral flavors and truncated electric fields $E^{ij} = 0, \pm 1$ on links or plaquettes. The local Hilbert space dimension is $2^8 \times 3^4$ before Gauss-law projection and is reduced by enforcing $G(\mathbf{r}) = 0$.

One Trotter step is

$$U(\Delta t) \approx \mathrm{e}^{-\mathrm{i}H_G\Delta t/2}\mathrm{e}^{-\mathrm{i}H_{\mathrm{dip}}\Delta t}\mathrm{e}^{-\mathrm{i}H_W\Delta t}\mathrm{e}^{-\mathrm{i}H_G\Delta t/2} + \mathcal{O}(\Delta t^3), \tag{63}$$

where $H_G = (U/2)\sum_{\mathbf{r}} G(\mathbf{r})^2$. A sequence of $N_T = 20$ to 60 steps is sufficient for the toy parameters used in the figures. The Trotter error scales as $N_T\Delta t^3\|[H_a,[H_b,H_c]]\|$. Gauge-violation error is monitored by $\langle G^2\rangle$. Measurement requires repeated estimates of Q_5, P^i, J^{ij}, and the boundary occupation. For a trapped-ion or neutral-atom implementation, the dipole constraint can be enforced energetically by a large U. For superconducting circuits, the same constrained dynamics can be implemented by parametrically driven pair hoppings.

The observable discriminant is

$$\Delta Q_5 \neq 0, \qquad \Delta P^i_{\text{bulk}} = 0, \qquad \int J^{ij} \neq 0, \qquad \int J^i_{\text{ordinary}} \approx 0. \tag{64}$$

This set of inequalities would show mobility transmutation in a finite simulator. It would not by itself prove the continuum anomaly coefficient; that requires the scaling and flux quantization checks described above.

18 Experimental and Synthetic Realizations

Several platforms can approximate the ingredients. Ultracold atoms in optical superlattices can implement staggered fermion chains, synthetic gauge fields, and constrained pair hopping. Neutral-atom arrays naturally realize Rydberg blockade constraints that can suppress isolated motion and allow composite motion. Trapped ions provide long-range programmable interactions suitable for small spectral-flow protocols. Superconducting circuits can implement digital Trotter steps and measure local constraints. Tensor-network emulation can reach larger one-dimensional or quasi-two-dimensional systems and is useful for the hinge cascade.

The most direct synthetic target is a coupled-wire realization. Each wire supports a chiral anomaly in an applied axial background. Interwire couplings are restricted to dipole-preserving pair transfers. The resulting array has lineon transport along wires and dipole motion transverse to them. A flux insertion through the array pumps Q_5, while current tomography distinguishes wire current from transverse dipole current. This setup uses the anisotropic u_a version of Eq. (20); it does not require full rotational symmetry.

Materials realizations are more speculative. Candidate systems would need chiral band crossings, long-lived approximate dipole conservation, and slow momentum relaxation. Gapless fracton spin liquids and constrained semimetals are possible directions, but the present paper does not identify a confirmed material. The effective theory is better viewed as a guide for synthetic platforms and controlled numerical experiments.

19 Limitations, No-Go Results, and Counterexamples

The construction has sharp boundaries. First, exact dipole conservation is incompatible with microscopic Lorentz invariance for charged local fermions without additional structure. Any relativistic notation used in the anomaly polynomial is shorthand for a nonrelativistic theory with coframes and a preferred foliation.

Second, a pure symmetric tensor scalar-charge theory does not automatically have a quantized axial anomaly proportional to $\mathcal{E}_{ij}\mathcal{B}^{ij}$. Such a term can appear in an effective action, but it is universal only after being embedded into a coframe theory with two-form curvatures or after an independent spectral-flow index is established.

Third, the fractonic chiral magnetic coefficient is an equilibrium coefficient. Dynamic homogeneous response depends on the order of limits, boundary relaxation, and weak dipole breaking. Experiments and simulations must therefore measure the flux-cycle index or static magnetization response rather than only a finite-frequency conductivity.

Fourth, disorder is harmless only when it preserves the relevant flux quantization and dipole constraint. Generic single-particle hopping breaks the symmetry and allows the anomaly-generated charge to relax into ordinary diffusion. The signature then becomes a crossover rather than a protected transport law.

Finally, the lattice construction is a regulator and proof of principle. It uses Wilson fermions and constrained pair hopping to avoid doubling and enforce multipole conservation. It does not prove that every fracton phase with chiral excitations realizes the same mixed anomaly. Distinct subsystem symmetries, non-Abelian dipoles, or noninvertible boundary sectors require separate analysis.

20 Discussion

The analysis supports a specific version of the proposed central conclusion. When chiral quantum matter is subject to exact dipole or higher-moment conservation, anomaly-generated charge is not forced to appear as an ordinary vector current. In the coframe dipole-gauge formulation, the mixed anomaly polynomial fixes a Ward identity in which axial charge pumping is tied to dipole curvatures. Hydrodynamics then converts this source into tensor currents, lineon propagation, surface dipole accumulation, and hinge inflow. This is anomaly-induced mobility transmutation.

The result is also constrained. The universal anomaly is not the most naive tensor expression one might write in the scalar-charge language. It is the cohomology class built from differential-form curvatures F^a, together with the no-go theorem that explains why a preferred spatial structure is necessary. This makes the theory less sweeping but more reliable. It identifies the background data required for quantization, the counterterms that shift consistent currents, and the circumstances in which the mobility anomaly index is meaningful.

Several directions are immediate. A complete subelliptic index theorem for fractonic chiral operators would put the spectral-flow argument on the same footing as the ordinary Dirac index. A non-Abelian extension could classify multipole anomalies in spin-orbit coupled semimetals. A Schwinger-Keldysh effective action with exact dipole gauge symmetry could determine all second-order transport coefficients and noise terms. Finally, finite quantum simulators can test the central mobility transmutation signature with present-day control requirements.

21 Conclusion

We have constructed a theoretical and computational framework for a fractonic chiral plasma. The main findings are: exact dipole conservation requires nonrelativistic spatial structure; a coframe dipole gauge theory admits a quantized mixed axial-dipole anomaly; the integrated anomaly defines a mobility-resolved flux index; the equilibrium response contains a fractonic chiral magnetic tensor current; and anomaly inflow can cascade from bulk to surface to hinge when mobility constraints block ordinary charge transport. The accompanying lattice model, numerical figures, and quantum-simulation protocol give controlled realizations of these statements. The resulting universality class is not merely a chiral plasma with slow diffusion. It is an anomalous quantum fluid in which symmetry and topology determine the mobility sector of the transported charge.

A Appendix A: Differential-Form Conventions

We use $F = \frac{1}{2}F_{\mu\nu}\mathrm{d}x^\mu \wedge \mathrm{d}x^\nu$ and $\int F/2\pi \in \mathbb{Z}$ for normalized $U(1)$ flux. The wedge product obeys $F^a \wedge F^b = F^b \wedge F^a$ because both forms have even degree. The component relation is

$$F^a \wedge F^b = \frac{1}{4}\epsilon^{\mu\nu\rho\sigma} F^a_{\mu\nu} F^b_{\rho\sigma}\, \mathrm{d}^4x. \tag{65}$$

The axial anomaly obtained from $I_6 = F_5 \wedge X_4/(2\pi)$ is $\nabla_\mu J^\mu_5 = X_4/(2\pi)$ in form notation, with the component normalization used in Eq. (23).

B Appendix B: Boundary Terms for Dipole Conservation

For a region Σ with boundary, Eq. (6) gives

$$\frac{\mathrm{d}Q_\Sigma}{\mathrm{d}t} = -\int_{\partial\Sigma} \mathrm{d}S_i\, \partial_j J^{ij}, \tag{66}$$

$$\frac{\mathrm{d}P^k_\Sigma}{\mathrm{d}t} = -\int_{\partial\Sigma} \mathrm{d}S_i \left(x^k \partial_j J^{ij} - J^{ik} \right). \tag{67}$$

These formulas are used in the numerical finite-difference checks. They also explain why surface dipole currents and hinge currents are not optional in an open system.

C Appendix C: Consistent and Covariant Currents

The consistent axial current is obtained by varying the regulated effective action. It satisfies Wess-Zumino consistency but may transform noncovariantly under vector or dipole gauge transformations. Adding a Bardeen-Zumino current shifts

$$J^\mu_{5,\mathrm{cov}} = J^\mu_{5,\mathrm{cons}} + K^\mu_{\mathrm{BZ}}, \tag{68}$$

where K^μ_{BZ} is a local polynomial in A, A^a, A_5. The transport formulas in Sections 8 and 9 use covariant currents because they are the currents measured by gauge-invariant probes. The integrated anomaly index is unchanged by this shift.

D Appendix D: Heat-Kernel Derivation of the Dipole Term

This appendix spells out the local calculation behind Eq. (23). The purpose is not to introduce a new regulator, but to show precisely where the dipole curvature enters the standard anomaly calculation and where the nonrelativistic background data are used. Work in Euclidean signature with a fixed clock form and spatial coframe. The regulated kinetic operator is

$$\mathcal{D} = \gamma^\mu \left(\nabla_\mu + \mathrm{i}QA_\mu + \mathrm{i}D_a A^a_\mu + \mathrm{i}Q_5\gamma_5 A_{5\mu}\right). \tag{69}$$

The internal matrices Q, D_a, Q_5 are taken Hermitian and mutually commuting in the minimal model. Noncommuting generalizations are possible, but then the anomaly polynomial is written with a symmetrized trace. The curvature of the non-axial connection is

$$\Omega_{\mu\nu} = \frac{1}{4}R_{\mu\nu ab}\gamma^{ab}\mathrm{i}Q\mathcal{F}_{\mu\nu}\mathrm{i}D_a F^a_{\mu\nu}, \tag{70}$$

where $\mathcal{F} = \mathrm{d}A - e_a \wedge A^a$ rather than $\mathrm{d}A$. This replacement is forced by dipole gauge invariance. Under $A \mapsto A - \lambda_a e^a$ and $A^a \mapsto A^a + \mathrm{d}\lambda^a$, the two terms in $\mathcal{F}$ cancel in flat torsionless space.

The square of the operator has the Laplace form

$$\mathcal{D}^\dagger\mathcal{D} = -g^{\mu\nu}\nabla^\Omega_\mu\nabla^\Omega_\nu + E, \tag{71}$$

with $E = \frac{1}{2}\gamma^{\mu\nu}\Omega_{\mu\nu}$ plus curvature terms that do not contain four gamma matrices. The axial Jacobian is

$$\delta_\theta \log\mathcal{J} = -2\mathrm{i}\int \mathrm{d}^4x\, e\,\theta(x) \lim_{M\to\infty} \mathrm{tr}\left[\gamma_5 \exp\left(-\frac{\mathcal{D}^\dagger\mathcal{D}}{M^2}\right)\right]. \tag{72}$$

The heat-kernel expansion gives

$$\mathrm{tr}\left[\gamma_5 \mathrm{e}^{-\mathcal{D}^\dagger\mathcal{D}/M^2}\right] \to \frac{1}{32\pi^2}\epsilon^{\mu\nu\rho\sigma}\,\mathrm{Tr}_{\mathrm{int}}\left[Q_5\left(Q\mathcal{F}_{\mu\nu} + D_aF^a_{\mu\nu}\right)\left(Q\mathcal{F}_{\rho\sigma} + D_bF^b_{\rho\sigma}\right)\right], \tag{73}$$

where the trace over spinor indices uses

$$\mathrm{tr}_\gamma\left(\gamma_5\gamma^{\mu\nu}\gamma^{\rho\sigma}\right) = 4\epsilon^{\mu\nu\rho\sigma}. \tag{74}$$

Expanding the internal trace yields the three gauge terms in Eq. (23). The mixed vector-dipole coefficient is

$$\mathrm{Tr}_{\mathrm{int}}(Q_5QD_a). \tag{75}$$

This object transforms as a spatial vector. It therefore vanishes in a rotation-invariant bulk unless an invariant vector is supplied by the phase itself. The heat-kernel computation does not hide this fact; it appears before any hydrodynamic approximation is made.

The calculation also clarifies regularization dependence. A Pauli-Villars regulator with the same dipole charges as the physical fermions preserves vector and dipole gauge invariance and assigns the anomaly to the axial current. A regulator that preserves axial symmetry instead would generate vector or dipole nonconservation. In a physical electromagnetic theory that option is unacceptable because $U(1)$ gauge invariance is a redundancy, not a global choice. The same logic applies to an exactly gauged dipole constraint. If the dipole symmetry is only global or emergent, one can move contact terms among Ward identities, but the spectral-flow index remains fixed when the background flux cycle is well defined.

For nonzero torsion the invariant curvature changes. If $\mathrm{d}e^a = T^a$, then

$$\delta\mathcal{F} = -\lambda_a T^a. \tag{76}$$

One can restore covariance by extending the transformation of A, adding a torsional Stückelberg field, or restricting to torsionless crystalline backgrounds. The paper uses the last option for quantized coefficients. Torsional responses are physically interesting, but they contain dimensionful coefficients analogous to the Nieh-Yan term and are not part of the minimal mobility anomaly index.

E Appendix E: Descent, Large Gauge Transformations, and Counterterms

Let

$$X_4 = \frac{k_{DD}}{2(2\pi)^2}\delta_{ab}F^a \wedge F^b. \tag{77}$$

The axial part of the anomaly polynomial is $I_6 = (F_5/2\pi) \wedge X_4$. A local choice of Chern-Simons form is

$$I_5^{(0)} = \frac{A_5}{2\pi} \wedge X_4. \tag{78}$$

Under the BRST rule $sA_5 = \mathrm{d}c_5$,

$$sI_5^{(0)} = \mathrm{d}\left(\frac{c_5}{2\pi}X_4\right), \qquad I_4^{(1)} = \frac{c_5}{2\pi}X_4. \tag{79}$$

The four-dimensional variation is

$$sW = 2\pi\mathrm{i}\int_{M_4} I_4^{(1)} = \mathrm{i}\frac{k_{DD}}{2(2\pi)^2}\int_{M_4} c_5\,\delta_{ab}F^a \wedge F^b. \tag{80}$$

Replacing the ghost with an axial gauge parameter gives the anomalous Ward identity. The Wess-Zumino consistency condition follows because $sX_4 = 0$ and $s^2A_5 = 0$.

Large gauge transformations impose the normalization. Let $F^a/2\pi$ be integral cohomology classes on a closed four-manifold. Then

$$\frac{1}{(2\pi)^2}\int F^a \wedge F^b \in \mathbb{Z} \tag{81}$$

for each pair a, b, with the integer determined by the intersection form. The exponentiated inflow action is invariant under $A_5 \mapsto A_5 + \mathrm{d}\theta_5$ with $\oint \mathrm{d}\theta_5 = 2\pi n$ if $k_{DD}\delta_{ab}$ is an integral bilinear form on the dipole charge lattice. This is the precise sense in which the mobility anomaly coefficient is quantized.

The most general local four-dimensional parity-odd counterterm built from one axial gauge field and dipole backgrounds has the schematic form

$$S_{\mathrm{ct}} = \frac{\mathrm{i}}{4\pi^2} \int \left[\alpha_1 A_5 \wedge A^a \wedge F_a + \alpha_2 A^a \wedge A_a \wedge F_5 + \alpha_3 A_5 \wedge A \wedge u_a F^a \right]. \tag{82}$$

The first two terms shift the consistent dipole and axial currents. They are not invariant under all large dipole gauge transformations unless the coefficients obey the same integrality conditions as the anomaly. They therefore cannot remove a nonzero cohomology class. The third term is absent in an isotropic phase because u_a is absent.

The consistent and covariant anomalies differ by the Bardeen-Zumino polynomial. For the dipole term, a convenient schematic current shift is

$$K^{\mu}_{\mathrm{BZ}} = \frac{k_{DD}}{8\pi^2} \epsilon^{\mu\nu\rho\sigma} \delta_{ab} A^a_\nu F^b_{\rho\sigma}. \tag{83}$$

Its divergence is a local polynomial. Adding it changes the local form of the current, but it does not change the integrated spectral flow because the latter is computed from fluxes on a closed cycle.

F Appendix F: Symmetric-Tensor No-Go Statement

The scalar-charge tensor gauge theory is indispensable for fracton kinematics, but it does not by itself provide a conventional chiral anomaly calculus. This appendix gives the detailed negative statement used in the main text. Consider a flat-space tensor gauge field with

$$B_0 \mapsto B_0 + \partial_t \alpha, \qquad B_{ij} \mapsto B_{ij} + \partial_i \partial_j \alpha. \tag{84}$$

The gauge-invariant fields $\mathcal{E}_{ij}$ and $\mathcal{B}_{ij}$ in Eq. (15) can form a scalar density $\mathcal{E}_{ij}\mathcal{B}^{ij}$ after choosing a spatial metric. However, three obstructions prevent this density from being a universal ABJ anomaly in the absence of extra structure.

First, $\mathcal{E}_{ij}\mathcal{B}^{ij}\mathrm{d}t\,\mathrm{d}^3x$ is not the pullback of a characteristic class of a principal bundle. It depends on the foliation and on the tensor gauge transformation with two spatial derivatives. A characteristic class can certainly be generalized, but then the generalized bundle and its large gauge transformations must be specified. The pure symmetric-tensor notation alone is insufficient.

Second, the natural chiral kinetic operators coupled to B_{ij} are not elliptic. A representative operator has transverse derivatives of order two and longitudinal derivatives of order one. The standard heat-kernel proof of the anomaly relies on a short-time expansion of an elliptic Laplace-type operator. Subelliptic operators can have indices, but their index depends on the bracket-generating distribution and boundary conditions. The coefficient is therefore not fixed by the tensor field alone.

Third, local counterterms can change $\int \mathcal{E}_{ij}\mathcal{B}^{ij}$ by improvement terms unless the background is embedded in a flux-quantized coframe theory. For example, the spatial integral of $B_{ij}\mathcal{B}^{ij}$ shifts under large tensor gauge transformations by boundary and winding data that are not captured by a single integer in the continuum scalar-charge description. This does not make the tensor response unphysical. It means that its coefficient is a transport coefficient of a model, not a cohomological anomaly coefficient.

The no-go theorem can be stated as follows. A four-dimensional local continuum theory whose only multipole background is B_0, B_{ij} and whose matter kinetic operator has no coframe projection, no foliation flux lattice, and no subelliptic index theorem cannot support a regulator-independent axial anomaly coefficient proportional only to $\mathcal{E}_{ij}\mathcal{B}^{ij}$. To evade the theorem one must add one of the missing ingredients. The coframe theory adds flux-quantized F^a. The Landau-level model adds a ladder algebra with a calculable subelliptic index. A lattice model adds a finite-dimensional regulator and a domain-wall spectral-flow count.

G Appendix G: Lattice Constraint Algebra and Continuity Check

The lattice Hamiltonian in Eq. (57) is designed so that the Gauss law generates the restricted operator algebra. Let $n_{\mathbf{r}} = c^\dagger_{\mathbf{r}} c_{\mathbf{r}}$ and define the discrete second derivative

$$\Delta_i \Delta_j E^{ij}_{\mathbf{r}} = E^{ij}_{\mathbf{r}+\hat{i}+\hat{j}} - E^{ij}_{\mathbf{r}+\hat{i}} - E^{ij}_{\mathbf{r}+\hat{j}} + E^{ij}_{\mathbf{r}}, \tag{85}$$

with the evident symmetrization for $i \neq j$. The local generator is

$$G_{\mathbf{r}} = n_{\mathbf{r}} - \Delta_i \Delta_j E^{ij}_{\mathbf{r}}. \tag{86}$$

An isolated hopping operator $c^\dagger_{\mathbf{r}+\hat{i}} c_{\mathbf{r}}$ has

$$[G_{\mathbf{x}}, c^\dagger_{\mathbf{r}+\hat{i}} c_{\mathbf{r}}] = (\delta_{\mathbf{x},\mathbf{r}+\hat{i}} - \delta_{\mathbf{x},\mathbf{r}}) c^\dagger_{\mathbf{r}+\hat{i}} c_{\mathbf{r}}, \tag{87}$$

so it changes the constraint unless accompanied by a gauge string whose endpoints carry the corresponding dipole flux. A pair hopping operator

$$c^\dagger_{\mathbf{r}+\hat{i}} c_{\mathbf{r}} c^\dagger_{\mathbf{r}'-\hat{i}} c_{\mathbf{r}'} \tag{88}$$

has zero net charge displacement and preserves total dipole moment. In the $U \to \infty$ projected Hilbert space, only operators commuting with all $G_{\mathbf{r}}$ survive at low energy.

The finite-difference numerical check mirrors this algebra. On a periodic $N \times N$ grid the code samples smooth arrays J^{xx}, J^{yy}, J^{xy} and sets

$$\dot{\rho} = -(\Delta_x^2 J^{xx} + \Delta_y^2 J^{yy} + 2\Delta_x \Delta_y J^{xy}). \tag{89}$$

Summing over the grid gives exact cancellation of every finite difference pair. Multiplying by x or y before summing also cancels on a periodic lattice when moment is understood modulo the system length. The saved file `data/conservation_check.csv` records the residuals, which are at floating-point roundoff. This check is included because it is easy for a numerical implementation of higher-rank continuity to preserve charge while accidentally violating dipole moment through boundary conventions.

The Wilson part of the Hamiltonian is vectorlike. The domain-wall mass produces chiral boundary modes, while the opposite wall or bulk regulator supplies the partner required by the lattice no-go theorem. During a flux cycle, levels cross from one boundary sector to another. This is how the lattice realizes anomaly inflow without ever defining a standalone single Weyl fermion on a closed lattice.

H Appendix H: Equilibrium Partition Function and Kubo Limit

The equilibrium derivation begins from the anomalous three-dimensional functional

$$W^{(3)}_{\text{anom}} = \frac{k_{DD}}{4\pi^2}\int_\Sigma \mu_5\, A^a \wedge F_a. \tag{90}$$

Here μ_5 is the holonomy of A_5 around the thermal circle. The dipole magnetization current is

$$\mathcal{J}_a = \frac{\delta W^{(3)}_{\text{anom}}}{\delta A^a} = \frac{k_{DD}}{2\pi^2}\mu_5 F_a + \frac{k_{DD}}{4\pi^2}\mathrm{d}\mu_5 \wedge A_a. \tag{91}$$

For homogeneous μ_5, only the first term remains. Pulling this two-form back to a spatial tensor sector gives Eq. (36). The term proportional to $\mathrm{d}\mu_5$ is an edge magnetization contribution and should not be confused with a bulk transport coefficient.

The Kubo formula is obtained by differentiating the retarded generating functional. Let h_{ij} be the source that couples to the symmetric tensor current. The generalized magnetic perturbation is

$$\delta\mathcal{B}^{ij}(\mathbf{k}) = \mathcal{P}^{ij,kl}(\mathbf{k})\,\mathrm{i}\epsilon_{kmn}k_m\,\delta h_{nl}(\mathbf{k}). \tag{92}$$

Then

$$G^R_{J^{ij}J^0_5}(\omega,\mathbf{k}) = -\mathrm{i}\int_0^\infty \mathrm{d}t\,\mathrm{e}^{\mathrm{i}\omega t}\langle[J^{ij}(t,\mathbf{k}), J^0_5(0,-\mathbf{k})]\rangle. \tag{93}$$

Projecting with $\mathcal{P}_{ij,kl}$ removes trace and longitudinal improvements. The equilibrium limit is

$$\lim_{\mathbf{k}\to 0}\lim_{\omega\to 0} G^R \tag{94}$$

if one asks for static susceptibility, while transport experiments often access

$$\lim_{\omega\to 0}\lim_{\mathbf{k}\to 0} G^R. \tag{95}$$

For scalar-charge hydrodynamics the density response contains

$$\frac{1}{-\mathrm{i}\omega + D_\perp k_\perp^4 + D_\parallel k_\parallel^2 + \Gamma_D}. \tag{96}$$

Thus the two limits agree only if $\Gamma_D = 0$ is taken after the static limit and if boundary leakage is negligible. This is the origin of the warning in the main text that the fractonic chiral magnetic effect is an equilibrium anomaly response, not a universal finite-frequency conductivity.

I Appendix I: Resource Estimates for the Simulation Protocol

The smallest circuit in Fig. 16 uses four matter sites and four truncated gauge variables. With two chiral flavors per matter site, the matter Hilbert space uses eight qubits. A three-level electric field can be encoded in two qubits with one unused state or in a native qutrit. The qubit encoding therefore uses sixteen physical two-level systems before ancillas for measurement. A native qutrit implementation uses eight qubits plus four qutrits.

The Hamiltonian is split into Wilson hopping, dipole pair hopping, gauge energy, and flux insertion pieces. If the largest local operator norm is $J_{\max}$, a second-order Trotter step has error bounded parametrically by

$$\epsilon_T \lesssim C N_T \Delta t^3 J_{\max}^3, \tag{97}$$

where C counts overlapping local terms. For the toy schedule $N_T = 40$, $J_{\max}\Delta t = 0.05$, and $C \sim 10^2$, the bound is conservative but below the percent level for the integrated charge. The experimentally relevant diagnostic is not the full wavefunction fidelity. It is the stability of the Ward-identity combination

$$\Delta Q_5 - \frac{k_{DD}}{(2\pi)^2} \int F^a \wedge F_a. \tag{98}$$

This observable can be estimated from repeated projective measurements of local occupation and gauge fields.

Gauge-constraint violations are monitored by

$$\epsilon_G(t) = \frac{1}{N} \sum_{\mathbf{r}} \langle G_{\mathbf{r}}^2(t) \rangle. \tag{99}$$

The simulation is accepted only in a window where $\epsilon_G \ll 1$, ΔP^i_{bulk} remains at measurement noise, and the tensor current signal exceeds the ordinary current leakage. Finite-size effects are large because the smallest system has only a few mobility sectors. The scaling test is therefore to repeat the protocol for longer coupled wires or larger plaquette arrays and verify that the integrated crossing count approaches an integer plateau.

J Appendix J: Figure-by-Figure Numerical Definitions

This appendix records the mathematical content of the sixteen figures so that the graphics can be read as part of the calculation rather than as decoration. The script uses deterministic arrays and a fixed random seed. Each plot is either exact within the effective theory, a finite-dimensional toy calculation, or a schematic map of definitions. Captions in the main text state which category applies.

Figure 1. The visual abstract is a three-dimensional schematic of the coframe theory. The cube represents a finite spatial region with a preferred coframe. Red points denote locally pumped axial charge, gold squares denote immobile charged excitations, and green paired markers denote mobile dipoles. The ordinary electromagnetic arrow and the dipole-curvature arrow correspond to the two terms $\mathcal{F}$ and F^a in the anomaly polynomial. The surface and hinge arrows show the orientation data used in the boundary descent.

Figure 2. The mobility graph is a directed graph of allowed channels. Solid arrows correspond to exact Ward-identity maps: axial source to local charge, local charge to dipole composite, and dipole composite to subdimensional current. Dashed arrows are relaxation channels that require a boundary, weak symmetry breaking, or a nonzero density of mobile impurities. The graph has no numerical weights because its purpose is to encode the selection rules.

Figure 3. The current hierarchy is the algebraic chain

$$Q \quad \to \quad P^i \quad \to \quad J^{ij} \quad \to \quad \partial_\mu J_5^\mu. \tag{100}$$

The figure separates the exact conservation law $\partial_t \rho + \partial_i \partial_j J^{ij} = 0$ from the anomalous axial law. This separation prevents a common mistake: the axial current can fail to be conserved while the electric charge and dipole moment remain exactly conserved.

Figure 4. The descent diagram visualizes the sequence

$$I_6 \to I_5^{(0)} \to I_4^{(1)} \to \nabla_\mu J_5^\mu. \tag{101}$$

The arrows are not fitted to data. They represent exterior differentiation and BRST variation. The bottom branch identifies the boundary current required by anomaly matching.

Figure 5. The field-geometry panels are generated from smooth analytic vector and tensor fields on a square grid. For the tensor panels, ellipses display the local eigenframe of a symmetric two-component field and quiver arrows display the projected curvature. The figure is meant to make clear why a rank-two field cannot be treated as an ordinary magnetic vector without choosing a projection.

Figure 6. The generalized Landau-level plot uses Eq. (41) with $B_D = 0.7$, $\alpha = 0.55$, and $v_z = 1$. For $n \geq 2$, the script evaluates

$$E_{n,\pm}(k_z) = \pm\sqrt{k_z^2 + 4\alpha^2 B_D^2 n(n-1)}. \tag{102}$$

The lowest two branches are chiral and gapless. The localization panel is a Gaussian lowest-state proxy. The bar chart records the crossing weights assigned to the mobility sectors in the toy regulator.

Figure 7. The spectral-flow figure computes a family of finite spectra

$$E_m(\phi) = 0.55\left(m + \frac{\phi}{2\pi} - 2\right) \tag{103}$$

and superposes two mobility-resolved crossing branches. The staircase inset counts zero crossings during the flux cycle. It is a discrete representation of Eq. (28), not a diagonalization of a large lattice Hamiltonian.

Figure 8. The response heat map is generated directly from

$$J_D = \frac{k_{DD}}{2\pi^2}\mu_5 B_D \tag{104}$$

with $k_{DD} = 2$. The line cuts verify the separate linearity in axial chemical potential and generalized magnetic field. This figure is exact within the equilibrium effective action.

Figure 9. The boundary-cascade figure uses the same cube geometry as Fig. 1 but highlights one surface and one hinge. A saved numerical profile,

$$\rho_{\text{edge}}(x, z) = \exp\left[-\frac{(x-L)^2 + (z-z_0)^2}{\ell^2}\right], \tag{105}$$

is written to `boundary_profile.csv`. The profile is used only as a visualization of localization.

Figure 10. The hydrodynamic-mode plot evaluates the real and imaginary parts of Eq. (60). The transverse comparison curve $-Dk_\perp^4$ is plotted against a reference ordinary diffusion curve $-D_2k_\perp^2$. The crossing of these scales identifies the momentum below which weak dipole breaking would dominate if present.

Figure 11. The quench dynamics use a smooth source $s(t) = \exp[-(t-4)^2/3]$. The axial charge is the cumulative integral of $s(t)$, the tensor current follows the ramp envelope, and the entanglement proxy is a saturating curve with a small decaying oscillation. These are effective-model time traces designed to test plotting, normalization, and conservation diagnostics.

Figure 12. Current tomography uses three fields on the same grid: a suppressed Gaussian ordinary current, a sinusoidal tensor-current channel, and an edge-localized hinge profile. The tensor panel overlays a quiver field obtained from numerical gradients. The corresponding CSV file contains $x, y, J_{\text{ordinary}}, J_{\text{tensor}}, J_{\text{hinge}}$.

Figure 13. The phase diagram is a regime map, not a fitted phase boundary. Its axes are dipole constraint strength and axial imbalance. The region labeled fractonic chiral plasma is the window where the constraint is strong enough to restrict isolated charge but not so strong that all mobile composites are confined.

Figure 14. The disorder scan distinguishes dipole-preserving disorder from explicit dipole breaking. The anomaly index is held fixed for preserving disorder, while the transport peak broadens. The dipole-breaking curve follows $\exp(-0.55w)$, representing loss of mobility-sector resolution as forbidden single-particle hopping grows.

Figure 15. The circuit diagram is a schedule for state preparation, Gauss-law energy evolution, Wilson hopping, dipole hopping, flux insertion, and measurement. It does not assume a specific hardware gate library. Its purpose is to show which observables must be measured after each flux step.

Figure 16. The research-landscape plot assigns schematic coordinates to adjacent fields. The axes are chirality/anomaly control and mobility restriction/boundary hierarchy. The proposed theory lies near the high-high corner because it combines both ingredients. The coordinates are qualitative and derive from Table 1.

K Appendix K: Observable Dictionary and Data Products

The following definitions are used consistently in the code and manuscript. The axial charge is

$$Q_5(t) = \sum_{\mathbf{r}} \left(n_R(\mathbf{r}, t) - n_L(\mathbf{r}, t) \right). \tag{106}$$

The electric charge is $Q = \sum_{\mathbf{r}} n(\mathbf{r})$. The dipole moment on an open lattice is

$$P^i(t) = \sum_{\mathbf{r}} r^i n(\mathbf{r}, t). \tag{107}$$

On a periodic lattice the same expression is used only for infinitesimal checks; the physical invariant is the exponentiated large-gauge operator

$$U_i = \exp\left(\frac{2\pi \mathrm{i}}{L_i} \sum_{\mathbf{r}} r^i n(\mathbf{r}) \right). \tag{108}$$

The tensor current is defined through the discrete continuity equation. Given a time step Δt,

$$\frac{\rho(t + \Delta t) - \rho(t)}{\Delta t} = -\Delta_i \Delta_j J^{ij}(t) + O(\Delta t). \tag{109}$$

This definition fixes only the double divergence of J^{ij}. The plotted current chooses the minimal-norm representative after removing transverse improvements. This choice is adequate for tomography but is not a separately gauge-invariant observable.

The mobility-resolved spectral count is obtained by assigning each crossing state a sector label α. In the toy model the labels are determined by the branch index. In a microscopic model they would be determined by matrix elements of projected displacement operators,

$$M^i_{mn} = \langle m | U_i^\dagger X^i U_i - X^i | n \rangle, \tag{110}$$

or by the support of the wave function on line, plane, or hinge submanifolds. The index is

$$\nu_{\text{mob}} = \sum_\alpha s_\alpha C_\alpha, \tag{111}$$

where C_α is the net crossing count in sector α.

The data files have the following content. `landau_spectrum.csv` stores the momentum and lowest chiral branch used in Fig. 6. `spectral_flow.csv` stores the flux and crossing count used in Fig. 7. `fme_response.csv` stores μ_5, B_D, J_D grid values for Fig. 8. `hydro_modes.csv` stores real and imaginary frequencies for Fig. 10. `quench_dynamics.csv` stores Q_5, P^x, J^{xx}, and the entanglement proxy for Fig. 11. `current_tomography.csv` stores spatial current maps for Fig. 12. `disorder_scan.csv` stores the disorder curves for Fig. 14. `conservation_check.csv` stores the residuals $\Delta Q, \Delta P^x, \Delta P^y$.

The numerical precision target is modest but explicit. Kinematic conservation checks should be at roundoff. Spectral-flow counts should be integer after crossing identification. Hydrodynamic curves should reproduce the analytic small-k expansion. The circuit diagram has no numerical fidelity claim. These distinctions matter because a publication-style theoretical paper should not present a stylized figure as a measurement.

L Appendix L: Assumption Ledger

This final technical appendix lists the assumptions under which the main statements are valid. It is included because the subject combines several effective descriptions that are sometimes used interchangeably in the literature. The conclusions of the paper are robust only when the relevant assumptions are kept attached to the corresponding result.

A1: Background geometry. The mixed axial-dipole anomaly is formulated on an Aristotelian or crystalline background with a clock form, spatial metric, and coframe. The coframe is not an optional notation. It supplies the internal index a, the dipole gauge transformation $A \mapsto A - \lambda_a e^a$, and the flux lattice needed for large gauge transformations. Removing this structure leaves a valid symmetric-tensor fracton theory, but not the same anomaly polynomial.

A2: Exact versus emergent symmetry. Quantized anomaly coefficients require exact vector and dipole gauge redundancies in the regulated theory. Emergent dipole conservation can produce the same hydrodynamic form over an intermediate time window, but the mobility index then becomes a prethermal or approximate diagnostic. If single-particle hopping is present with rate Γ_D, the tensor response crosses over to ordinary diffusion at times $t \gtrsim \Gamma_D^{-1}$.

A3: Regulator. The anomaly coefficient is computed with a regulator that preserves ordinary charge gauge invariance and dipole gauge invariance. The axial symmetry is the anomalous symmetry. A different regulator can redistribute the local anomaly among consistent currents, but any regulator that changes the integrated flux index has changed the theory or the allowed background bundle.

A4: Mobility sector resolution. The mobility anomaly index is tensor-valued before contraction. Its sector labels are meaningful only when the Hamiltonian or background distinguishes dipole orientation, lineon axis, planon leaf, or hinge support. In a strongly mixing phase with no stable sector labels, the integrated axial charge pumping can remain quantized while the phrase mobility transmutation becomes a statement about relaxation channels rather than a sharp index.

A5: Boundary matching. The boundary no-go theorem assumes a unique gapped symmetric boundary without intrinsic topological order. A topologically ordered boundary, a symmetry-broken boundary, or a boundary with spatial modulation can match the same anomaly without a simple chiral hinge mode. The hinge cascade is therefore a natural and explicit solution of anomaly matching, not the only logically possible solution.

A6: Numerical status. The numerical calculations are finite controlled demonstrations. They verify equations, conservation laws, spectral-flow counting, and response formulas in toy models. They do not claim experimental observation, large-scale many-body thermalization, or material prediction. The role of the code is reproducibility and falsifiability of the manuscript's internal calculations.

A7: Terminology. The term fractonic chiral plasma is retained because the paper derives a consistent setting in which chiral anomaly pumping coexists with multipole-constrained transport. The term mixed axial-multipole anomaly is used only for the cohomological obstruction represented by I_6. The term fractonic chiral magnetic effect is used only for the equilibrium tensor response derived from the anomaly functional and Kubo limit. These restrictions are part of the result.

M Appendix M: Reproducibility

The project contains the following files. The main source is `main.tex`. Section sources are in `sections/`. The bibliography database is `references.bib`; the compiled manuscript uses an embedded bibliography to avoid external-tool ambiguity. Figure code is `scripts/generate_figures.py`.

Generated figures are in `figures/`. Numerical arrays are in `data/`. The reproducibility notes are in `README.md`.

To regenerate the computational artifacts, run

```
python scripts/generate_figures.py
```

from the project root. To compile with a full TeX installation, run

```
latexmk -pdf main.tex
```

or use the bundled Codex LaTeX compiler described in the README.

References

[1] S. L. Adler, Axial-vector vertex in spinor electrodynamics, *Physical Review* **177**, 2426 (1969).

[2] J. S. Bell and R. Jackiw, A PCAC puzzle: $\pi^0 \to \gamma\gamma$ in the sigma model, *Nuovo Cimento A* **60**, 47 (1969).

[3] K. Fujikawa, Path-integral measure for gauge-invariant fermion theories, *Physical Review Letters* **42**, 1195 (1979).

[4] K. Fukushima, D. E. Kharzeev, and H. J. Warringa, The chiral magnetic effect, *Physical Review D* **78**, 074033 (2008), arXiv:0808.3382.

[5] D. T. Son and P. Surowka, Hydrodynamics with triangle anomalies, *Physical Review Letters* **103**, 191601 (2009), arXiv:0906.5044.

[6] D. E. Kharzeev, J. Liao, S. A. Voloshin, and G. Wang, Chiral magnetic and vortical effects in high-energy nuclear collisions, *Progress in Particle and Nuclear Physics* **88**, 1 (2016), arXiv:1511.04050.

[7] H. B. Nielsen and M. Ninomiya, Absence of neutrinos on a lattice. I. Proof by homotopy theory, *Nuclear Physics B* **185**, 20 (1981).

[8] M. Pretko, Subdimensional particle structure of higher rank $U(1)$ spin liquids, *Physical Review B* **95**, 115139 (2017), arXiv:1604.05329.

[9] M. Pretko, Generalized electromagnetism of subdimensional particles: A spin liquid story, *Physical Review B* **96**, 035119 (2017), arXiv:1606.08857.

[10] M. Pretko and L. Radzihovsky, Fracton-elasticity duality, *Physical Review Letters* **120**, 195301 (2018), arXiv:1711.11044.

[11] A. Gromov, Towards classification of fracton phases: The multipole algebra, *Physical Review X* **9**, 031035 (2019), arXiv:1812.05104.

[12] K. Slagle, A. Prem, and M. Pretko, Symmetric tensor gauge theories on curved spaces, *Annals of Physics* **410**, 167910 (2019), arXiv:1807.00827.

[13] M. Pretko, X. Chen, and Y. You, Fracton phases of matter, *International Journal of Modern Physics A* **35**, 2030003 (2020), arXiv:2001.01722.

[14] A. Jain and K. Jensen, Fractons in curved space, *SciPost Physics* **12**, 142 (2022), arXiv:2111.03973.

[15] X. Huang, A Chern-Simons theory for dipole symmetry, *SciPost Physics* **15**, 153 (2023), arXiv:2305.02492.

[16] P. Glorioso, J. Guo, J. F. Rodriguez-Nieva, and A. Lucas, Breakdown of hydrodynamics below four dimensions in a fracton fluid, *Nature Physics* **18**, 912 (2022), arXiv:2105.13365.

[17] D. Rovere, Anomalies in covariant fracton theories, *Physical Review D* **110**, 085012 (2024), arXiv:2406.06686.

[18] S. Shimamura, Anomaly of subsystem symmetries in exotic and foliated BF theories, arXiv:2404.10601 (2024).

[19] N. Niggemann, M. Adhikary, Y. Schaden-Thillmann, and J. Reuther, Gapless fracton quantum spin liquid and emergent photons in a 2D spin-1 model, arXiv:2508.06605 (2025).

[20] R. Shen, T. Chen, T. Tai, J. M. Koh, P. Ghaemi, and C. H. Lee, Simulating condensed matter physics on quantum hardware, arXiv:2606.02721 (2026).

[21] T. Hayata and A. Yamamoto, Quantum anomaly for benchmarking quantum computing, arXiv:2603.03697 (2026).